ChemComm

Check for updates

Recent advances in nanomaterial-enabled chemiresistive hydrogen sensors

Yao Yang Liu,[a] Zhong Li,*[ab] Yi Liang,[a] Tao Tang,[a] Jing Hao Zhuang,[a] Wen Ji Zhang,[a] Bao Yue Zhang [ID][c] and Jian Zhen Ou [ID]*[ac]

With the growing adoption of hydrogen energy and the rapid advancement of Internet of Things (IoT) technologies, there is an increasing demand for high-performance hydrogen gas (H_2) sensors. Among various sensor types, chemiresistive H_2 sensors have emerged as particularly promising due to their excellent sensitivity, fast response times, cost-effectiveness, and portability. This review comprehensively examines the recent progress in chemiresistive H_2 sensors, focusing on developments over the past five years in nanostructured materials such as metals, metal oxide semiconductors, and emerging alternatives. This review delves into the underlying sensing mechanisms, highlighting the enhancement strategies that have been employed to improve sensing performance. Finally, current challenges are identified, and future research directions are proposed to address the limitations of existing chemiresistive H_2 sensor technologies. This work provides a critical synthesis of the most recent advancements, offering valuable insights into both current challenges and future directions. Its emphasis on innovative material designs and sensing strategies will significantly contribute to the ongoing development of next-generation H_2 sensors, fostering safer and more efficient energy applications.

1. Introduction

With the rapid development of technology, the world is currently faced with a severe energy crisis resulting from excessive exploitation and utilization of non-renewable energy sources. Hydrogen gas (H_2) has been generally regarded as a crucial component of the global energy system due to its abundance, efficiency, cleanliness and recyclability.[1] In essence, hydrogen energy sources significantly contribute to the sustainable development of our world. However, H_2 has a high burning velocity, a wide flammable range (4–75 vol%), a low ignition energy (0.017 mJ), and a high heat combustion (142 kJ g^{-1}), which makes it extremely dangerous during production, transportation, storage, and utilization processes.[2] In addition, its colorless, odorless, and tasteless properties pose challenges for human sensory detection.[3] Therefore, the research and utilization of H_2 sensors are indispensable for achieving real-time and comprehensive detection of H_2.

In recent years, researchers have been dedicated to the development of H_2 sensors with heightened sensitivity, expanded detection range, accelerated response time, improved stability, enhanced gas

selectivity, and near-room-temperature operability to achieve timely, precise, and convenient H_2 concentration detection. To date, the commercially available H_2 sensors are mainly divided into eight categories based on their fundamental principles and detection methods, including work function, acoustic, optical, catalytic, thermal conductivity, mechanical, electrochemical and resistance types.[2] Among these types, work function based H_2 sensors are micromachinable, small in size, have low cost, and can be mass-produced; however, they are susceptible to drift and exhibit a hysteresis effect.[4] Although acoustic sensors with high sensitivity can operate in the absence of oxygen (O_2) from room temperature to 100 °C, it is challenging to operate at a higher temperature without interference from humidity and temperature.[2,5] In terms of optical sensors, there is no source of ignition in explosive atmospheres and the utilization of optical fiber transmission makes them immune to electromagnetic interference, but the stringent requirements on the preparation process, complex structure, high cost, and challenging signal monitoring restrict their large-scale industrial application.[6] Catalytic sensors are suitable for the detection of high concentrations of H_2 ($> 4\%$) with exceptional stability and prolonged lifespan, but they do possess certain limitations including elevated operational temperatures, increased power consumption, limited capability to differentiate between other combustible gases, and a requirement for 5–10% O_2.[7] Furthermore, the thermal conductivity sensors have a higher detection limit and a poor selectivity for gases with high thermal conductivity.[2] And the mechanical sensors also have disadvantages including slow response time, susceptibility to

[a] Key Laboratory of Advanced Technologies of Materials, Ministry of Education, School of Materials Science and Engineering, Southwest Jiaotong University, Chengdu 610031, China. E-mail: zhong.li@swjtu.edu.cn, jzou@swjtu.edu.cn

[b] Jiangsu Key Laboratory of Advanced Structural Materials and Application Technology, Nanjing Institute of Technology, Nanjing 211167, China

[c] School of Engineering, RMIT University, Melbourne, Victoria 3000, Australia. E-mail: jianzhen.ou@rmit.edu.au

poisoning and hydrogen-induced aging effects.[2] Compared with the above-mentioned H_2 sensors, both electrochemical and chemiresistive H_2 sensors are considered as state-of-the-art technologies for H_2 sensing nowadays.[8] Nevertheless, the electrochemical sensors are highly susceptible to ambient conditions (temperature, pressure, humidity and oxygen), difficult to integrate, and have rather complicated systems that require high fabrication costs.[9] In contrast, chemiresistive H_2 sensors, which operate by using sensitive materials to react with H_2 and convert chemical reactions into electrical signals (resistance or conductance), have been considered particularly promising for development due to their high sensitivity, fast response, long lifetime, low cost, wide operating temperature range, simple production, and portable applications.[8,10]

There has also been a significant emphasis on chemiresistive H_2 sensors in numerous studies due to the above-mentioned advantages. Generally, the performance of H_2 sensors relies upon the reactions between H_2 and sensing materials. Therefore, accurate processing of the dimensions and shapes of materials is essential for improving sensing performance. With the development of nanotechnology, numerous nanomaterials have been employed for H_2 sensing due to their high surface area-to-volume ratio, abundant surface active sites, high carrier mobility, and interesting physical and chemical properties.[11–15] On the one hand, palladium (Pd) can easily react with H_2 inducing the formation of PdH_x with a higher resistivity even at room temperature.[16] Thus, Pd-based H_2 sensors have been widely studied owing to their excellent sensing properties, especially their high selectivity and room temperature operation. However, the interference of O_2 molecules in the ambient air significantly hinders the reaction between H_2 and Pd resulting in degraded performance of the sensor in terms of sensitivity and response speed,[17] while the sluggish diffusion of H atoms in Pd lattices also leads to severe hysteresis of the sensor.[18] These challenges present obstacles to the advancement of high-performance H_2 sensor technology. Therefore, researchers are currently focusing on enhancing the sensing characteristics of Pd-based H_2 sensors by investigating various aspects such as Pd nanostructures, Pd-based bimetals, and Pd-based composites. On the other hand, metal oxide semiconductor (MOS)-based sensors, which rely on the modulation of electrical signals resulting from the interaction between H_2 and chemisorbed oxygen on the surface of MOSs, have also been extensively employed for H_2 sensing in diverse applications. Nevertheless, the adsorption and desorption of O_2 of MOS-based sensors typically require elevated temperatures exceeding 200 °C,[19] thereby restricting their commercial application due to the increased power consumption and reducing their selectivity owing to the high reactivity of other interfering gases induced by elevated temperatures. Consequently, to tackle these challenges, researchers have devised diverse effective approaches, encompassing the design of nanostructures, functionalization by noble metals, doping of elements, and constructing heterojunctions. Besides, emerging materials also demonstrate remarkable H_2 sensing capabilities at room temperature, such as graphene, carbon nanotubes (CNTs), transition metal disulfides (TMDs), and MXenes. Thus, owing to technological advancements, the scope of research on hydrogen-sensitive materials is continuously broadening.

In this review, we classify chemiresistive H_2 sensors into three categories from the perspective of sensitive materials: metal-based, MOS-based, and other materials (graphene, CNTs, TMDs, and MXenes). Firstly, we present a detailed introduction to the gas-sensing mechanisms employed by each type of chemiresistive H_2 sensor. Subsequently, we provide a comprehensive overview of the latest research progress and development strategies for high-performance chemiresistive H_2 sensors, focusing primarily on elucidating the physicochemical mechanisms that contribute to enhanced sensing performance through various improvement methods. We particularly emphasize the intricate relationship between sensing performance and factors such as structural characteristics, surface modifications, and chemical and electrical properties. Finally, we conclude the status of H_2 sensor research, point out existing limitations, and provide prospects for future research directions.

2. Metal-based H_2 sensors

Among various metals for H_2 sensors, Pd has been known as the most appealing material due to its unique ability to reversibly and selectively form PdH_x in the presence of H_2 under ambient conditions at room temperature. Therefore, there have been developed numerous Pd-based H_2 sensors, including Pd nanostructures, Pd-based bimetals and Pd-based composites. Additionally, except for Pd, Pt also exhibits a gas response to H_2. O_2 molecules in the surrounding air are readily dissociated and adsorbed onto the surface of Pt, leading to an increase in Pt resistance due to electron scattering on the adsorbed oxygen molecules. Subsequently, upon exposure to H_2, the catalytic conversion of adsorbed oxygen into water occurs while H_2 chemisorbs onto the surface of Pt forming Pt–H, resulting in a decrease in resistance unlike Pd.[8,20] The response time of Pt towards H_2 exposure was observed to be faster compared to that of Pd under the same operating conditions.[20] However, a significant limitation of Pt-based sensors is that they exhibit identical resistance change for H_2 concentrations exceeding 0.1% due to early saturation, which greatly limits their practical applications.[20,21] Consequently, limited subsequent research has been conducted on pure Pt-based sensors. In this section, we provide a detailed discussion on sensing mechanisms and recent advancements related to Pd-based H_2 sensors.

2.1. Sensing mechanisms for Pd-based H_2 sensors

In general, the sensing mechanisms of Pd-based H_2 sensors are attributed to the formation of PdH_x. H_2 molecules are easily adsorbed on the surface of Pd and dissociated into H atoms at room temperature (eqn (1) and (2)). Then, the H atoms spontaneously and selectively diffuse into the octahedral interstitial sites of the face-centered cubic (FCC) Pd lattice (Fig. 1a).[22] In the Pd–H system, PdH_x usually has two phases (α phase and β phase) due to the different H_2 pressures.[1] When exposed to an H_2 pressure below 1%, Pd undergoes partial filling of its interstitial sites, leading to the formation of a solid-solution phase (α phase, eqn (3)).[22] With the increase of H_2 pressure (1% < [H_2] < 2%), the interaction between dissolved H atoms in Pd metal becomes more
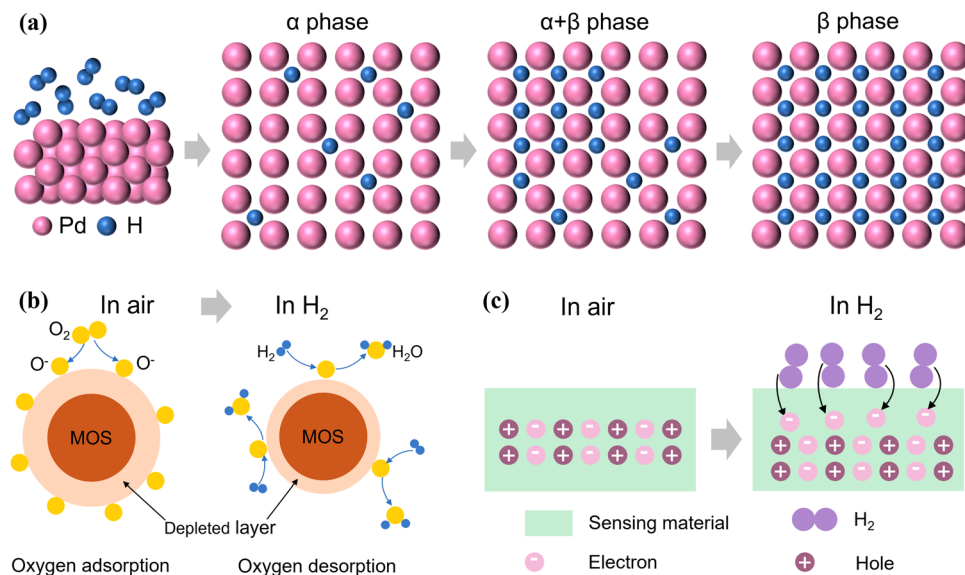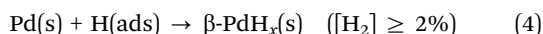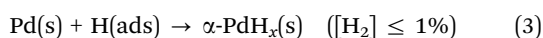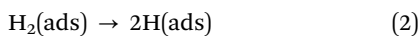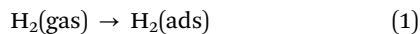
Fig. 1 (a) Schematic of hydrogen diffuse into the Pd lattice. (b) Schematic of chemisorption based on MOSs. (c) Schematic of physisorption.

pronounced, which induces the first transition in the PdH_x matrix.[23,24] Simultaneously, nucleation of the β phase occurs within the α phase and subsequently the α and β phases coexist until a complete phase transition from α to β ($[H_2] \geq 2\%$, eqn (4)).[24] Moreover, both α-PdH_x and β-PdH_x exhibit a higher resistivity compared to Pd, because the H atoms occupied in the interstitial sites act as scattering sites impeding the movement of free electrons.[8] Generally, the increase in resistivity resulting from the formation of PdH_x is considered the primary sensing mechanism for most of the Pd-based H_2 sensors. However, the further formation of β phase induces significant volume expansions in the Pd lattice, which results in irreversible structural changes in Pd. Consequently, achieving linear detection of high concentrations of H_2 ($[H_2] \geq 2\%$) while maintaining excellent long-term stability poses a formidable challenge. Additionally, the presence of interfering gases, which is inevitable in practical applications, will influence the permeability of H_2. The carbon monoxide (CO), nitrogen oxides, or hydrocarbon instead of H_2 competitively absorb on the site of Pd and occupy the active sites, thereby reducing the H_2 permeability into the Pd and further reducing the selectivity.[25–27] Therefore, in practical applications, it is also necessary to consider how to eliminate the influence of interfering gases.

$$H_2(gas) \rightarrow H_2(ads) \tag{1}$$

$$H_2(ads) \rightarrow 2H(ads) \tag{2}$$

$$Pd(s) + H(ads) \rightarrow \alpha\text{-}PdH_x(s) \quad ([H_2] \leq 1\%) \tag{3}$$

$$Pd(s) + H(ads) \rightarrow \beta\text{-}PdH_x(s) \quad ([H_2] \geq 2\%) \tag{4}$$

2.2. Pd nanostructures

With the development of nanomaterials and nanotechnology, numerous Pd nanostructures, including Pd nanoparticles (NPs),[28] Pd nanowires (NWs),[29–31] Pd nanosheets,[32] and Pd nano hollow shells,[33] have been explored for H_2 sensors. Pd nanostructures have significant advantages for H_2 sensing applications due to their high surface area-to-volume ratio, electron transport ability, high porosity, and exposure of high-energy facets that are catalytically active.[31]

Among them, Pd NWs have been the most extensively studied. It was previously reported that precise control and design of the size of Pd NWs are critical for achieving highly efficient H_2 sensing.[34] However, conventional lithography techniques are incapable of fabricating Pd NWs with a diameter smaller than 10 nm and also entail relatively high costs. Solution-phase synthesis enables the production of Pd NWs exhibiting an exceptionally high aspect ratio and small diameter, but they are typically capped with surfactants or ligands that pose challenges in their removal and interfere with sensing applications.[35] As a consequence, to address the aforementioned limitations, Kumar et al.[31] showed a solution-phase synthesis of Pd NWs with an ultrathin diameter smaller than 5 nm and treated with an ultraviolet (UV-O) source to remove the ligands attached to their surface. Subsequently, a comparative analysis was conducted to evaluate the H_2 sensing performance pre and post UV-O treatment, revealing that the sensor subjected to UV-O treatment exhibited enhanced sensitivity along with accelerated response and recovery speed. Additionally, the UV-O-treated sensor displayed response and recovery time of 3.4 and 11 s to 1% H_2 with high selectivity to H_2 in comparison with CO, CO_2, and CH_4. After being exposed to 100 ppm CO for 2 minutes, which was much higher than the allowable concentration in the ambient environment, the response to 100 ppm H_2 only decreased by 10%. However, the author only mentioned short-term repeatability within 30 minutes, neglecting to investigate the long-term stability, which was one of the primary concerns in practical applications. In general, the high properties of the Pd NW-based sensor can be ascribed to its ligand-free surface and ultrathin diameter.

Interestingly, Jo et al.[29] developed a phase-transition-inhibited Pd NW sensor with a linear response at 4% H_2. The
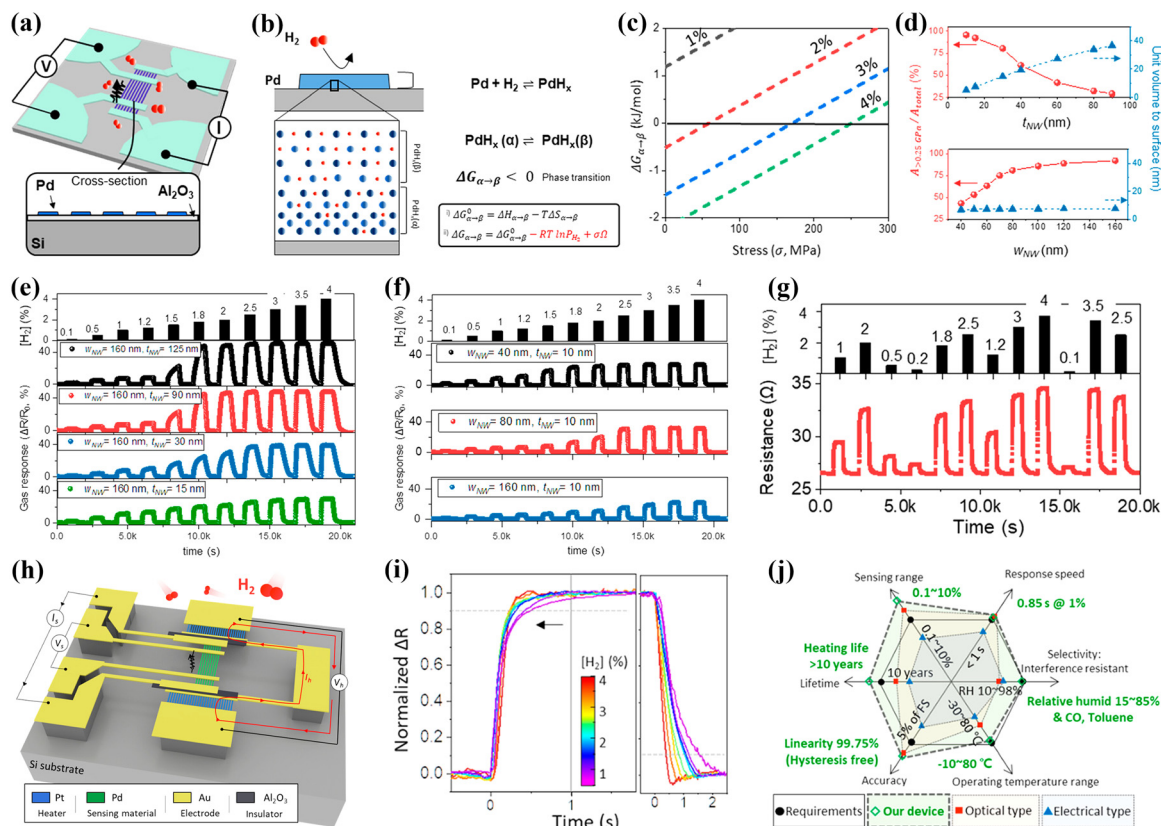
Fig. 2 (a) Schematic illustration of the Pd NW H$_2$ sensor. (b) Schematic of the internal lattice structure of Pd NWs with two phases and the thermodynamic quantities related to H$_2$ pressure and stress for the phase transition of PdH$_x$ from α to β. (c) Gibbs free energy of the PdH$_x$ phase transition varied with stress (σ) at four different concentrations of H$_2$. (d) Curves of $A_{>0.25\,GPa}/A_{total}$ and unit volume to surface concerning t_{NW} or w_{NW}. (e) Response–recovery curves of Pd NW sensors with different t_{NW} and fixed w_{NW} (160 nm) to different H$_2$ concentrations ranging from 0.1 to 4%. (f) Response–recovery curves of Pd NW sensors with different w_{NW} and fixed t_{NW} (10 nm) to different H$_2$ concentrations ranging from 0.1 to 4%. (g) Response–recovery curves of Pd NW sensors to various random H$_2$ concentrations (w_{NW} = 160 nm, t_{NW} = 15 nm). Reproduced with permission from ref. 29. Copyright 2022 American Chemical Society. (h) Schematic representation of the Pd nanoelectromechanical H$_2$ sensing device and its structural characteristics for rapid H$_2$ detection. (i) Response/recovery time for Pd NW sensors of different H$_2$ concentrations from 1–4%. (j) Chart of the six required performances in H$_2$ detection compared the four different types of devices. Reproduced with permission from ref. 30. Copyright 2023 American Chemical Society.

H$_2$ sensing device, as illustrated in Fig. 2a, comprised a precisely aligned array of Pd NWs serving as the sensing material along with four electrodes. Since the bottom of Pd NWs was fixed to the substrate, compressive stress was generated near the substrate to partially inhibit volume expansion when H diffused into the interstitial sites of Pd. The inhibition of the PdH$_x$ phase transition in the high-stress region can be explained by the change of the free energy equation (Fig. 2b). According to ideal solid solution absorption effects, free energy was directly influenced by H$_2$ pressure (P_{H_2}) and internal stress of the solid. The internal stress restricted the diffusion of atoms within the solid, leading to a change in chemical potential and an enhancement of α-phase PdH$_x$ stability. Consequently, when sufficiently high stress was generated in Pd NWs, diffusion of H atoms became challenging, thereby achieving an inhibitory effect on phase transition. Furthermore, it was determined that a critical stress of at least 0.25 GPa was required in PdH$_x$ to successfully inhibit the phase transition at 4% H$_2$ (Fig. 2c) and it was presumed that regions with a high $A_{>0.25\,GPa}/A_{total}$, especially above 90%, are imperative for effectively inhibiting

phase transition due to variations in stress induced by the size of the Pd NWs. As shown in Fig. 2d, the Pd NWs with width (w_{NW}) greater than 160 nm and thickness (t_{NW}) less than 15 nm were suitable for phase transition inhibition and fast response time. To verify the theoretical predictions experimentally, they compared the H$_2$ response of Pd NWs with different widths and thicknesses. The Pd NWs with a width of 160 nm and a thickness exceeding 15 nm exhibited an abrupt increase in sensitivity at 1.5% of H$_2$, indicating the initiation of β-phase transition and then showed identical gas responses from 2 to 4% of H$_2$ because of the saturation of H content in the nanowire (Fig. 2e). Moreover, a similar phenomenon was also displayed in Pd NWs with a thickness of 10 nm and a width below 160 nm (Fig. 2f). Therefore, the Pd NWs with a width of 160 nm and a thickness of 10 nm exhibited linear response and repeatable performance to H$_2$ concentrations from 0.1 to 4% (Fig. 2f and g).

It has already been above-mentioned that the phase transition is accompanied by an increase in resistance; however, as the H$_2$ concentration further increases, it is difficult to

distinguish the concentration of H_2 due to the saturation of H_2 resulting in the saturation of resistance. Therefore, it becomes challenging to achieve linear detection up to 10% H_2. Meanwhile, the application of thermal energy to activate Pd has been recognized as an efficacious approach to accelerate the response rate without material engineering by improving the H_2 adsorption efficiency and impeding the phase transition of PdH_x.[36] Accordingly, the following year, Jo et al.[30] designed a coplanar Pt NW heater-integrated sensing architecture for optimal thermal activation of pure Pd NWs to achieve a subsecond (~ 0.6 s) response time and a linear detection of up to 10% H_2. The structure of the device can maximally expose the reaction sites of Pd NWs and form a uniform temperature in the sensing elements by constructing a conductive heat transfer design (Fig. 2h). Therefore, this sensor displayed a fast response time of 0.6 s in the concentration range of 1–4%, a wide detection range of 0.1–10% with 99.75% linearity and durable heating operation in a wide temperature range (-10 to 80 °C) with high repeatability (>104 cycles) and a long heating lifetime (>10 years) (Fig. 2i and j). It's worth noting that the influence of CO and high humidity can be ignored due to the high operating temperature, which lowered the adsorption of CO and condensation of water. However, the detection of high concentrations of H_2 is always accompanied by a poor long-term stability, which was not investigated in this paper. On the whole, the synergistic effect of nanostructures and thermal activation can significantly enhance the H_2 sensing characteristics.

2.3. Pd-based bimetals

To mitigate the irreversible damage caused by the α-β phase transition of PdH_x in Pd-based H_2 sensors, it is common practice to employ Pd-based bimetals as hydrogen-sensitive materials instead of pure Pd. This strategy has been shown to effectively mitigate phase changes by occupying Pd's interstitial sites with different metal atoms.[29] Furthermore, the Pd-based bimetals have superior activity for surface reactions relative to pure Pd. Commonly, the metal elements used to form bimetals with Pd are Pt, Au, Ag, Sn and Ni.[37–44]

Owing to the same FCC structure and minimal lattice mismatch (0.77%),[45] Pt is a promising candidate for the synthesis of Pd-based bimetals. One recent advance in Pd-based bimetals was the demonstration of a facile synthesis of ultra-small bimetallic nanoparticles (BM-NPs) of PdPt produced within porous ion-exchange polymers to create high-performance H_2 sensors that enable wireless detection reported by Koo et al. (Fig. 3a).[40] Herein, the porous ion-exchange polymer of imidazolium-functionalized triptycene polyether sulfone (ITPES) enabled homogeneous diffusion and immobilization of an ionic metal precursor of complementary charge into the polymer matrix, thus achieving precise regulation of the size (down to 1 nm) and composition of BM-NPs, which was critically important for sensing performance. Furthermore, upon exposure to H_2, due to the synergistic effect of PdPt NPs, two reactions occurred: (1) the removal of surface-adsorbed oxygen resulted in a decrease in resistance, and (2) H_2 adsorption led to an elevation in resistance (Fig. 3b). The two reactions occurred

simultaneously, with the former dominating the resistance at high levels of $[H_2]$, while the latter prevailed at low levels of $[H_2]$. Thus, the resistance of the ITPES-PdPt NPs sensors decreased when exposed to H_2 concentrations above 100 ppm and then switched to an increase in resistance with H_2 exposures below 16 ppm (Fig. 3d). Based on these results, the ITPES-PdPt NP-based sensor demonstrated remarkable stability and excellent H_2 sensing properties with a response of 15.7% to 4% H_2 and a low detection limit of 0.4 ppm (Fig. 3c–e). However, a linear gas response had not been achieved. Therefore, the reliability of the sensor necessitated further enhancement. In general, it is imperative to enhance the H_2 sensing performance through the synthesis of small-sized (below a few nanometers) Pd-based bimetallic NPs exhibiting exceptional surface activity.

In addition, various Pd-based bimetals can improve H_2 sensing performances by constructing nanostructures with high specific surface area and multiple active sites. In this regard, Song et al.[43] firstly fabricated hollow Pd–Sn alloy nanotubes (NTs) with a high surface area and ultrafine grain sizes by relying on particle migration and coalescence of neighboring particles. As shown in Fig. 3f, the SEM image revealed the shape of the Pd–Sn NTs in a hollow morphology having high porosity with superfine grain sizes. Besides, compared to Pd–Sn alloy nanofilms (NFs), Pd NFs and Sn NFs, the Pd–Sn NTs exhibited excellent sensitivity toward H_2 (0.00005–3%) and a high response of 9.27% to a concentration of H_2 (3%) at room temperature due to the highly porous structure with smaller nanograins offering more exposed active sites and higher gas accessibility (Fig. 3g and h). From the results, it is an efficient method to develop Pd-based bimetals with special nanostructures for the improvement of the H_2 sensing performance.

However, the above-mentioned sensors exhibit long response/recovery times, which limits their application. Usually, appropriately increasing the operating temperature of the sensor will accelerate the diffusion of H_2 resulting in a faster response/recovery speed. For instance, Liu et al.[41] proposed a heating operation mode of the Pd/Ni-based H_2 sensor integrating with a Pt heating wire. They found that the Pd/Ni film demonstrated a short response/recovery time of 7/6 s to 2% H_2 at the optimal temperature of 75 °C. In addition, Deepti et al.[37] reported that Pd–Au alloy exhibited a significantly reduced response/recovery time (7/50 s) to 2% H_2 at 250 °C due to the ion irradiation, whereas the pristine sample displayed long response/recovery time (114/78 s). This improvement can be attributed to the ion-irradiation induced defects, which enhance the rate of H_2 absorption. Nevertheless, the elevated operating temperature of 250 °C is accompanied by high power consumption, thereby impeding their commercial applications. Therefore, further investigation is imperative to facilitate the attainment of rapid response and recovery capabilities for this type of sensor while operating at near room temperature.

2.4. Pd-based composites

The combination of Pd with other materials induces synergistic effects, thus improving stability, enhancing sensitivity, and accelerating the response/recovery speed of the Pd-based
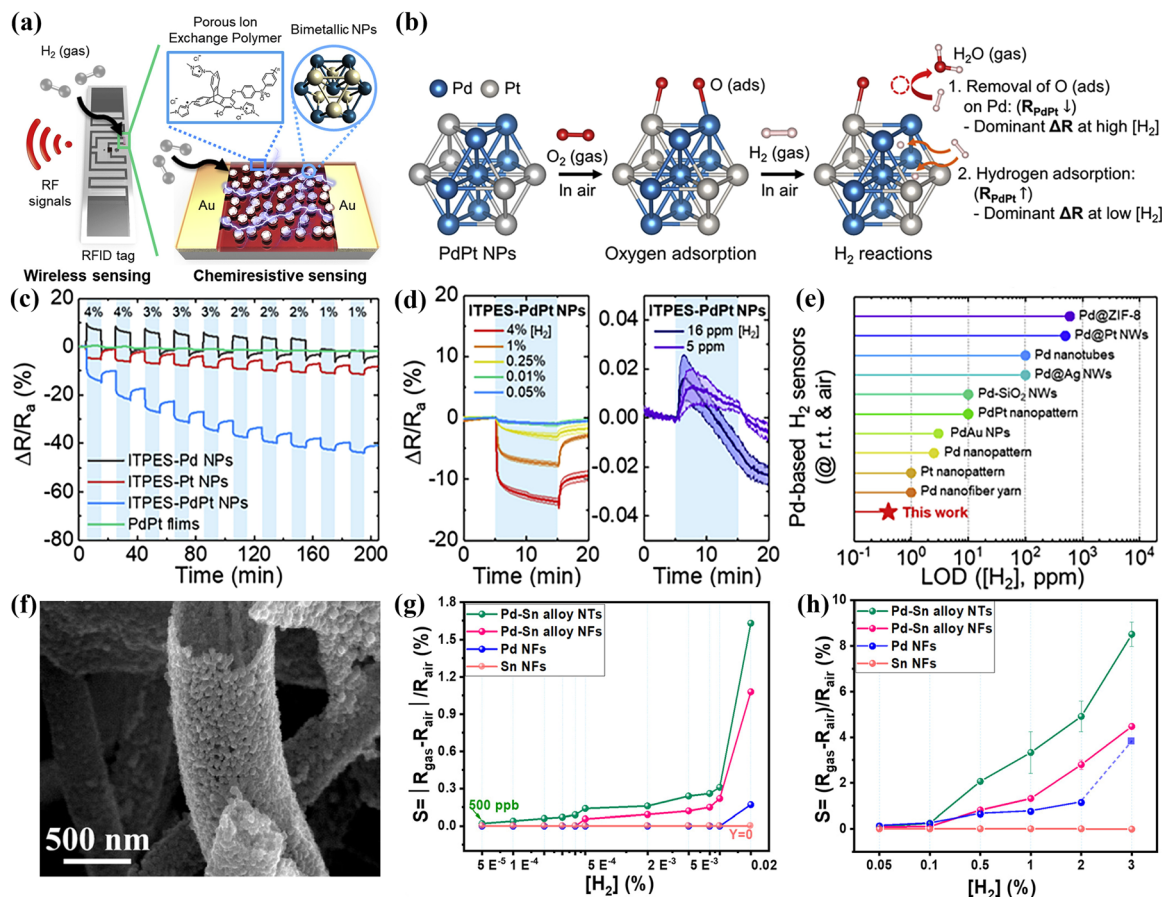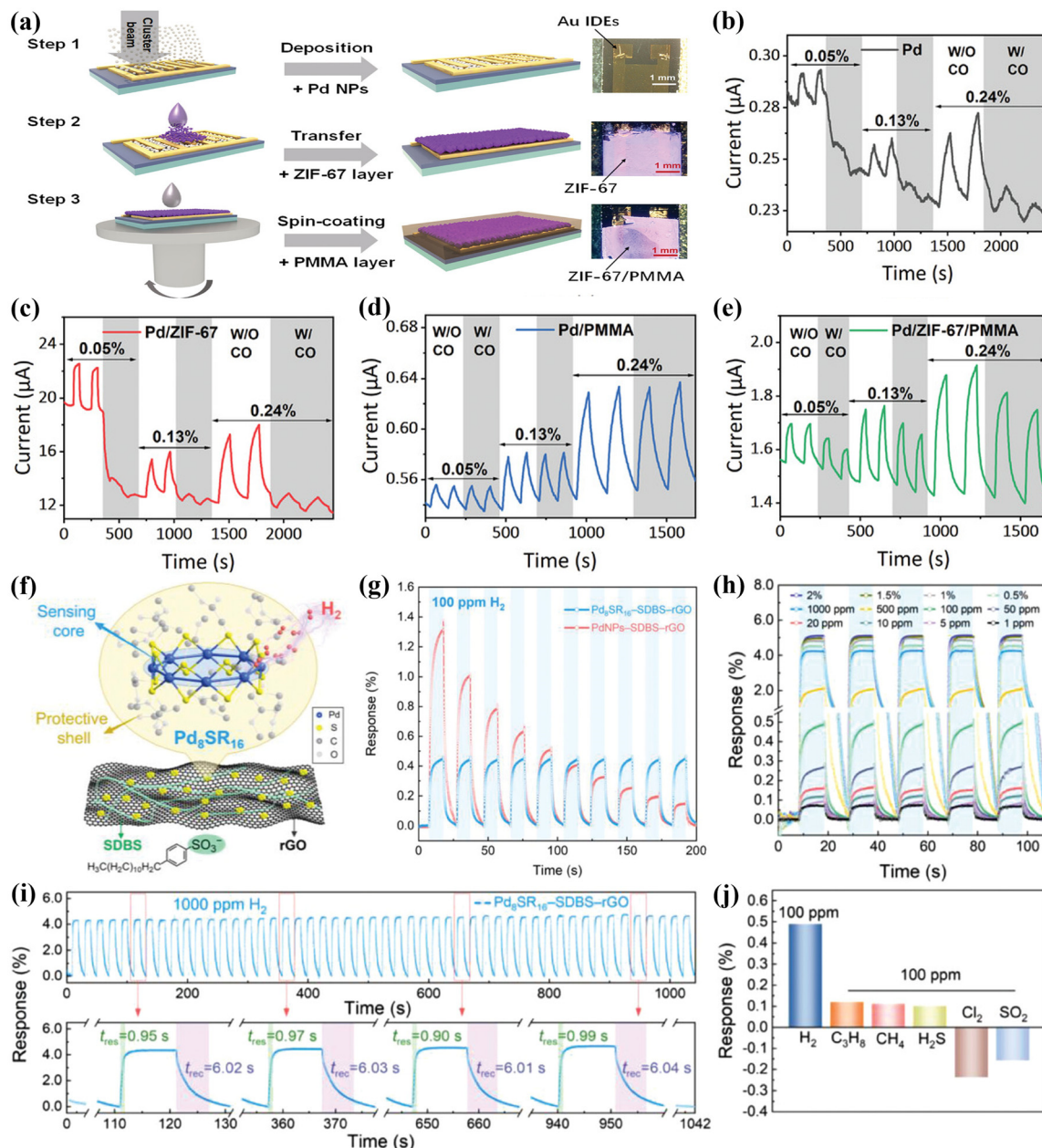
Fig. 3 (a) Schematic illustration of the chemiresistive H_2 sensing system with wireless detection. (b) Schematic illustration of the H_2 sensing mechanisms of ITPES-PdPt NPs. (c) Response–recovery curves of ITPES-Pd NPs, ITPES-Pt NPs, ITPES-PdPt NPs, and PdPt films at room temperature to different H_2 concentrations ranging from 1 to 4%. (d) Response–recovery curve of ITPES-PdPt NPs to 5 and 16 ppm and 0.05%, 0.01%, 0.25%, 1%, and 4% of H_2 at room temperature. (e) Comparison of the detection limits of different Pd-based H_2 sensors. Reproduced with permission from ref. 40. Copyright 2020 Elsevier. (f) Schematic illustration of the synthesis process for Pd–Sn alloy NTs. (g) Normalized response (S) versus H_2 concentrations for Pd–Sn alloy NTs, Pd–Sn alloy NFs, Pd NFs, and Sn NFs at H_2 concentrations of 0.5–200 ppm and (h) 5000–3000 ppm. Reproduced with permission from ref. 43. Copyright 2022 American Chemical Society.

sensors by using Pd-based composites. To date, many Pd-based composites have been developed, effectively addressing numerous challenges encountered in practical applications.[46–51]

For instance, Xing et al.[50] developed an H_2 sensor by using Pd NPs decorated on the carbon/nitrogen porous framework. It exhibited a wide concentration range of 200 ppm to 40% ($S \approx$ 73.8% and $T_{res} \approx 9$ s) H_2 sensing at room temperature, showing exceptional long-term stability with reliable H_2 sensing maintained for up to 142 days. The exceptional performance can be attributed to the presence of Mott–Schottky heterojunctions between Pd NPs and N-doped carbon materials and the three-dimensional (3D) porous structures, which show excellent catalytic activity and provide abundant surface sites for gas diffusion and adsorption due to their large specific surface area. This result demonstrates the efficacy of incorporating other materials with Pd to enhance stability and reduce response/recovery time, thereby offering an efficient approach for improving Pd-based H_2 sensors.

However, Pd-based H_2 sensors are susceptible to poisoning and deactivation due to the adsorption of CO, nitrogen oxides,

or hydrocarbons.[27,52] Due to the relatively smaller size of H_2 compared to other molecules, applying a polymer coating on H_2 sensing materials can effectively act as a molecular sieve. However, this approach usually results in an extended response time and a compromised sensitivity of the sensor. Therefore, to overcome these issues, Xie et al.[49] constructed a triple-layer Pd nanocluster film-metal organic framework (MOF)-polymer hybrid nanocomposite for H_2 detection. Among them, the polymethyl methacrylate (PMMA) membrane acted as a molecular sieve, while the zeolitic imidazole framework-67 (ZIF-67) film served as an interfacial layer between the Pd NC film and the protective PMMA layer (Fig. 4a). To confirm that this structure had a good ability to resist CO poisoning without causing degradation of the sensor performance, they conducted an H_2 sensing test in a CO background for various sensor types, including Pd, Pd/ZIF-67, PD/PMMA, and Pd/ZIF-67/PMMA. As shown in Fig. 4b and c, the presence of ZIF-67 film greatly enhanced the sensitivity of the sensor; however, upon exposure to CO, their performances were significantly diminished. However, even in the presence of CO, both Pd/PMMA and

Fig. 4 (a) Schematic illustration of the fabricated Pd/ZIF-67/PMMA sensor. Response–recovery curves of (b) Pd, (c) Pd/ZIF-67, (d) Pd/PMMA, and (e) Pd/ZIF-67/PMMA to H_2 with different concentrations along with 1% CO gas. Reproduced with permission from ref. 49. Copyright 2022 Wiley-VCH GmbH. (f) Structure diagram for Pd_8SR_{16}–SDBS–rGO used for H_2 sensing. (g) Response–recovery curves for Pd_8SR_{16}–SDBS–rGO and PdNPs–SDBS–rGO sensors to 100 ppm H_2 at room temperature. (h) Response–recovery curve of the Pd_8SR_{16}–SDBS–rGO sensor to different H_2 concentrations ranging from 1 ppm to 2%. (i) 50-cycle response–recovery curve and response/recovery time for the Pd_8SR_{16}–SDBS–rGO sensor to 1000 ppm H_2 at room temperature. (j) Selectivity of Pd_8SR_{16}–SDBS–rGO towards H_2 in comparison with interfering gases including C_3H_8, CH_4, H_2S, Cl_2, and SO_2. Reproduced with permission from ref. 46. Copyright 2024 Wiley-VCH GmbH.

Pd/ZIF-67/PMMA exhibited consistent responses upon the introduction of the PMMA membrane (Fig. 4d and e). Hence, these results indicated that the obtained Pd/ZIF-67/PMMA hydride nanostructure effectively mitigated performance degradation associated with a single polymer coating and synergistically combined the satisfactory CO-poisoning resistance conferred by the PMMA membrane with improved sensing performance provided by the ZIF-67 film. In conclusion, Pd/ZIF-67/PMMA demonstrated optimal comprehensive performance owing to its unique nanocomposite structure.

In addition to the formation of bimetals, Pd nanoclusters (NCs) also exhibit the ability to impede phase transitions through diverse H_2 binding mechanisms.[46,53] Moreover, metal NCs display atomic precision in composition, exceptional efficiency in metal utilization, and highly controllable geometries; thus, they emerge as promising candidates for sensing

Table 1 Summary of the sensing properties of Pd-based H_2 sensors

Material	Morphology	Conc. (%)	Tem. (°C)	Res. (%)	T_{res}/T_{rec} (s)	MDL (ppm)	Ref.
Pd	Hollow shells	1	RT	60	16/—	75	33
Pd	Nanoparticles	1	RT	30.65	11.6/15.7	—	31
Pd	Nanowires	1	RT	1.7	3.4/101	10	31
Pd	Nanowires	4	RT	35.9	21/270	1000	29
Pd	Nanosheets	1	RT	0.4	50/60	5	51
Pd	Nanowires	1	RT	0.34	12/28	200	35
Pd–Sn	Nanotubes	2	RT	4.8	20.2/17.9	1	43
PdPt	Nanoparticles	1	RT	7.56	92/304	0.4	40
Pd/Ni	Film	2	75	3.17	7/6	4000	41
Pd–Au	Film	2	250	9.1	7/50	—	37
MWCNT@Pd	Nanosheets	1	RT	3.6	74/25	5	51
Pd@rGO	Nanowires	1	RT	2.06	52/45	20	35
Pd@rGO@ZIF-8	Nanowires	1	RT	2.17	5/31	20	35
Pd$_8$SR$_{16}$–SDBS–rGO	Nanoclusters	0.1	RT	4	0.9/6	1	46
Pd–rGO	Nanoparticles	2	RT	14.8	73/126	25	48

Conc.: gas concentration; Tem.: operating temperature of the sensor; Res.: response of the sensor and response is defined as $(R_{gas} - R_{air})/R_{air} \times 100\%$; T_{res}: response time of the sensor; T_{rec}: recovery time of the sensor; MDL: minimum detection limit of the sensor; Ref.: reference; -: not reported; RT: room temperature (~ 25 °C); MWCNT: multiwalled carbon nanotube.

applications.[54] However, attaining stable existence for pure metal nanoclusters has proven to be a formidable challenge due to their elevated surface energy and reactivity.[55] Recently, a new advance of the Pd NC-based composites in H_2 sensing was reported by Chen *et al.*[46] They introduced thiolate-protected Pd nanoclusters (Pd$_8$SR$_{16}$), which unveiled the first-time application in H_2 sensing, showing the significant potential for rapid detection. Amongst others, the synergistic interaction between metal and ligand of Pd$_8$SR$_{16}$ resulted in the formation of an intermediate palladium–hydrogen–sulfur (Pd–H–S) state during H_2 adsorption. This state preserved the Pd–H binding while preventing excessive interaction, achieving a balance that reduced the activation energy required for H_2 desorption and facilitating highly reversible and rapid response/recovery. Furthermore, the Pd$_8$SR$_{16}$ as H_2 sensing sites were deposited on a sodium dodecylbenzene sulfonate/reduced graphene oxide (SDBS–rGO) carrier layer. The resulting Pd$_8$SR$_{16}$–SDBS–rGO sensor (Fig. 4f) effectively mitigated the restrictions associated with conventional Pd-based sensors across varying H_2 concentrations, including durability degradation or failure arising from excessive Pd–H binding or phase transitions. As shown in Fig. 4g, compared to the PdNPs–SDBS–rGO sensor, the Pd$_8$SR$_{16}$–SDBS–rGO sensor exhibited consistent signal stability across 10 cycles at a low H_2 concentration of 100 ppm, owing to the protection of thiolate. Additionally, the Pd$_8$SR$_{16}$–SDBS–rGO sensor displayed a wide detection range of H_2 concentrations from 1 ppm to 2% (Fig. 4h) and showed a stable and prompt response (t_{res} = 0.95 s) and recovery (t_{rec} = 6 s) at 1000 ppm H_2 (Fig. 4i). The practical application of this sensor effectively mitigated the interference from other gases due to the superior selectivity (Fig. 4j). Therefore, this study demonstrated the practicality of using ligand-protected metal nanoclusters for gas sensing in the real-world. From this perspective, researchers can employ diverse materials in conjunction with Pd to fulfill the practical application demands of H_2 sensing.

Currently, significant advancements have been achieved in the research on Pd-based H_2 sensors. The suppression of the phase transition can be effectively achieved through the design of devices and construction of bimetals, while the selectivity of the sensor has been enhanced through the incorporation of polymer coatings. Table 1 summarizes the sensing performance of Pd-based sensors in recent years. These sensors all exhibit high H_2 sensing performances, in terms of sensitivity, response/recovery speed, and detection limit. However, to mitigate the risk of H_2 explosions, it is imperative to reduce the response/recovery time for concentrations exceeding 1% H_2 to below 1 s. Therefore, further investigation is warranted to develop Pd-based H_2 sensors with faster response/recovery speed.
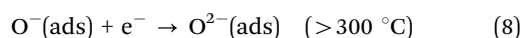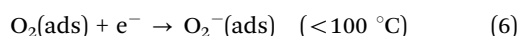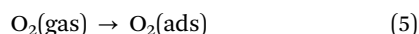
3. MOS-based H_2 sensors

The MOS-based resistive gas sensors have attracted considerable attention owing to their remarkable stability, high sensitivity, rapid response/recovery time, low cost, and simple manufacturing process,[10,56,57] rendering them a primary research focus for H_2 sensors. However, the gas sensitivity of MOS-based sensors relies on the redox reaction with adsorbed oxygen, enabling electron exchange with a diverse range of gases and inherently limiting gas selectivity. Simultaneously, in order to ensure enough carriers entering the conduction band for active participation in the reaction, a substantial number of MOS-based gas sensors necessitate elevated operating temperatures exceeding 200 °C.[10,19] The elevated operating temperature not only increases power consumption, impacts device integration, and compromises the gas selectivity of the sensor but also provides an additional ignition source, thereby posing safety hazards in proximity to combustible gases. Moreover, prolonged exposure to elevated temperatures can have a detrimental impact on the long-term stability of sensors by attenuating their sensitivity. Thus, in recent years, extensive research efforts have aimed at enhancing the gas selectivity and reducing the operational temperature of MOS-based H_2 sensors. In this section, we elucidate the fundamental sensing mechanisms and present
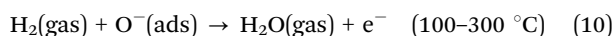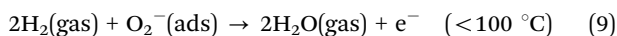
recent advancements in the development of MOS-based H_2 sensors, focusing on MOS nanostructures, modification of noble metal NPs, doping of elements, and MOS-based composites.

3.1.   Sensing mechanisms for MOS-based H_2 sensors

In general, the mechanism of MOS-based H_2 sensors is a change of electrical signals (current or resistance) caused by the inter-action between H_2 and chemisorbed oxygen on the surface of MOSs. The reception of H_2 signals in the air background by MOSs primarily relies on two reactions that occur on the surface of MOSs: O_2 adsorption leading to the formation of reactive oxygen species, and subsequent reaction between these reactive oxygen species and H_2 (Fig. 1b). The O_2 in the air readily absorbs onto the surface of the sensing materials, acting as an acceptor of electrons and dissociating on the surface of MOSs to capture electrons from the conduction band, resulting in the formation of species such as O_2^-, O^-, and O^{2-}. The adsorption reaction of oxygen is temperature-dependent (eqn (5)–(8)).[58,59]

$$O_2(gas) \rightarrow O_2(ads) \qquad (5)$$

$$O_2(ads) + e^- \rightarrow O_2^-(ads) \quad (<100\ ^\circ C) \qquad (6)$$

$$O_2^-(ads) + e^- \rightarrow 2O^-(ads) \quad (100–300\ ^\circ C) \qquad (7)$$

$$O^-(ads) + e^- \rightarrow O^{2-}(ads) \quad (>300\ ^\circ C) \qquad (8)$$

MOSs can be classified as either n-type or p-type, depending on whether the dominant carriers are electrons or holes. In the case of n-type MOSs, the adsorbed oxygen on the surface of the MOSs acts as a defect site and induces the Fermi level pinning effect. This effect leads to a reduction in electron density on the surface of MOSs, thereby forming an electron depletion layer (EDL) around the MOSs with a high potential barrier. The resistances of MOSs are significantly increased by the EDL, which arises from the reduction in net carrier density and the formation of potential barriers at the adsorption sites.[8,11] When MOSs are exposed to H_2, a reducing gas, H_2, reacts with the adsorbed oxygen to generate water and release free electrons (eqn (9) and (10)).[60] Consequently, the thickness of the EDL decreases, accompanying the decrease of the resistance of the MOS hydrogen gas sensors.[61] Upon re-exposure to atmospheric conditions, chemisorbed oxygen is formed as O_2 from the air gets adsorbed onto the surface of n-type MOSs again, increasing in resistance.

$$2H_2(gas) + O_2^-(ads) \rightarrow 2H_2O(gas) + e^- \quad (<100\ ^\circ C) \qquad (9)$$

$$H_2(gas) + O^-(ads) \rightarrow H_2O(gas) + e^- \quad (100–300\ ^\circ C) \qquad (10)$$

On the other hand, p-type MOSs exhibit an opposite beha-vior to n-type MOSs. The combination of adsorbed oxygen and electrons will generate additional holes on the surface of the p-type MOSs, thereby forming a hole accumulation layer (HAL). However, the reaction of H_2 with adsorbed oxygen effectively neutralizes these holes by releasing electrons, leading to a reduction in the thickness of the HAL and an increase in resistance. Subsequently, upon interaction between MOS-based sensors and H_2 followed by re-exposure to air, atmospheric

oxygen is reabsorbed to capture electrons from the conduction band, resulting in chemisorbed oxygen generation on the surface of the material and subsequent restoration of the surface space charge layer.[11,62] Therefore, it is imperative for both n-type and p-type MOS-based materials to possess a large surface area and a high reactivity to analytes, thereby augmenting their sensing properties.[63]

3.2.   MOS nanostructures

It is worth noting that MOS-based sensors rely on the gas–solid interfacial reaction between the target gas and the active sites on the surface of MOS, and thus the precise structural engineering of MOSs in terms of size and shape plays a crucial role in enhancing sensor properties. Consequently, many researchers have dedi-cated themselves to designing MOS-based nanostructures. At present, the common morphology design of MOS-based sensing materials includes nanoparticles,[64] nanospheres,[65] nanowires,[66] nanorods,[67] nanofilms,[68] nanosheets,[69] and nanoflowers.[70]

Among them, NPs and nanospheres exhibit high surface-to-volume ratios; however, their tendency to agglomerate can lead to a reduction in active sites. For instance, Zhu et al.[65] studied the effects of three representative nanostructures on H_2 sensing behaviors. As shown in Fig. 5a(i)–(iii), the three nanostructures namely solid spheres (0-SnO_2), nanoneedle-assembled nano urchins (1-SnO_2), and nanosheet-assembled nanoflowers (2-SnO_2) were synthesized by a facile hydrothermal method. The three SnO_2-based sensors were exposed to 400 ppm H_2 at different operating temperatures from 200 to 500 $^\circ C$ in air, and the highest responses for 0-SnO_2, 1-SnO_2, and 2-SnO_2 were estimated to be 12, 15, and 22 at the optimal operating temperature of 350 $^\circ C$ (Fig. 5b). Among them, the nanosheet-assembled nanoflowers displayed superior sensing perfor-mance owing to their abundant active absorption sites, whereas the solid spheres showed the lowest sensitivity due to their densely packed structures. Interestingly, it was observed that the three sensors demonstrated enhanced sensitivity under vacuum at the same conditions compared to the atmospheric environment (Fig. 5c). The first principles calculations revealed that the H_2 molecule preferred to directly adsorb on the surface of SnO_2 and transferred more electrons. According to the above results, it was revealed that a direct interaction between H_2 and SnO_2 took place in the absence of oxygen.

Additionally, one-dimensional (1D) nanostructures have garnered significant attention owing to their high surface-to-volume ratios and high porosity, including nanofibers, nano-wires, and nanorods. Recently, Tran et al.[67] demonstrated the role of aspect-ratio-controlled shape/size ZnO nanorods in H_2 sensing. As depicted in Fig. 5d, the three different aspect-ratio-controlled ZnO nanorods were synthesized by the thermal decomposition method at various annealing temperatures (350, 450, and 550 $^\circ C$), and the aspect ratio decreased with increasing temperature. The ZnO nanorods synthesized through thermal decomposition at 350 $^\circ C$ exhibited the highest aspect ratio ($\sim$6.25) among all tested samples, which demon-strated superior H_2 sensing capabilities with a response of approximately 483% to 80 ppm H_2 at 180 $^\circ C$ (Fig. 5e and f). Hence, the enhanced H_2 sensing response of the ZnO@350
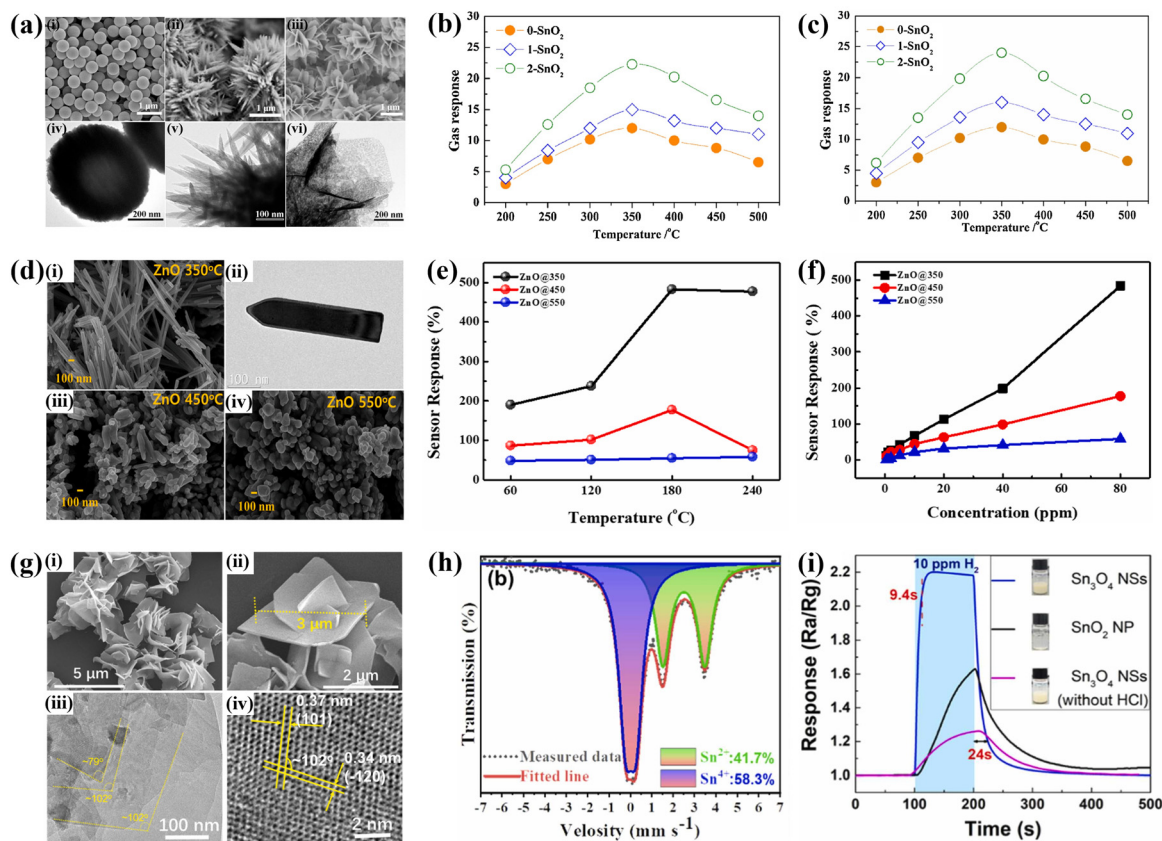
Fig. 5 (a) SEM and TEM images of SnO$_2$ samples: (i) and (iv) solid spheres, (ii) and (v) nanoneedle-assembled nano urchins, and (iii) and (vi) nanosheet-assembled nanoflowers. (b) Response of the three sensors exposed to 400 ppm H$_2$ at different operating temperatures (from 200 to 500 °C) in air. (c) Response of the three sensors exposed to 400 ppm H$_2$ at different operating temperatures (from 200 to 500 °C) in a vacuum. Reproduced with permission from ref. 65. Copyright 2018 Elsevier. (d) SEM and TEM images of aspect-ratio-controlled ZnO nanostructures: (i) and (ii) ZnO@350, (iii) ZnO@450, and (iv) ZnO@550. (e) Response of aspect-ratio-controlled ZnO nanostructures to 80 ppm H$_2$ at different operating temperatures from 60 to 240 °C. (f) Response of aspect-ratio-controlled ZnO nanostructures to different H$_2$ concentrations from 0.5 to 80 ppm at the optimal operating temperature of each sensor (ZnO@350 and ZnO@450: at 180 °C; ZnO@550: at 240 °C). Reproduced with permission from ref. 67. Copyright 2024 Elsevier. (g) (i) and (ii) SEM images of Sn$_3$O$_4$ nanosheets at different magnifications, (iii) TEM image of Sn$_3$O$_4$ nanosheets, (iv) HRTEM image of Sn$_3$O$_4$ nanosheets. (h) Room-temperature Sn Mössbauer spectroscopy. (i) Response–recovery curves of pristine and Sn^{2+}-deficient Sn$_3$O$_4$ as well as commercial SnO$_2$ towards 10 ppm H$_2$. Reproduced with permission from ref. 69. Copyright 2024 Elsevier.

sensor can primarily be attributed to its high aspect ratio morphology, which promoted the formation of oxygen vacancies and provided a greater number of active sites for gas adsorption.

Furthermore, Liu *et al.*[69] developed ultra large Sn$_3$O$_4$ nanosheet hierarchies with (010)-facet exposure and surface Sn^{2+}-deficiency *via* a facile hydrothermal method, which displayed excellent H$_2$ sensing performance due to the thermodynamic stability in the SnO phase and the existence of oxygen vacancies. Fig. 5g revealed that the Sn$_3$O$_4$ nanosheets with ultra-large two-dimensional (2D) structures were hierarchically assembled into a flower-like morphology and reflected the crystal growth orientation. It was confirmed that the exposed surface can be indexed as the (010) facet because the two sets of lattice fringes with *d*-spacings of 0.37 nm and 0.34 nm can be correspondingly indexed to the (101) and (−102) planes of the monoclinic Sn$_3$O$_4$ (Fig. 5g(iv)). Furthermore, as shown in Fig. 5h, the atomic ratio of Sn^{2+}/Sn^{4+} was approximately 41.7/58.3, demonstrating the deficiency of Sn^{2+} in Sn$_3$O$_4$, which can

be attributed to etching of HCl. Finally, they compared the H$_2$ sensing performance of the pristine and Sn^{2+}-deficient Sn$_3$O$_4$ nanosheets as well as the commercial SnO$_2$ nanopowders when exposed to 10 ppm H$_2$. The results showed that the Sn^{2+}-deficient Sn$_3$O$_4$ nanosheets consistently exhibited superior sensitivity and response/recovery speed compared to the other samples (Fig. 5i). Herein, the hierarchical structure of the Sn$_3$O$_4$ nanosheets facilitated rapid gas–solid interfacial contact reactions and fast release of target gases, while the Sn^{2+}-deficient (010) surface of Sn$_3$O$_4$ nanosheets offered abundant active adsorption sites for H$_2$ molecules. Therefore, the nanofilms or nanosheets have been used for H$_2$ sensing due to their large lateral size with numerous active absorption sites.

However, the challenges of low sensitivity, poor selectivity, and high operating temperature persist in pure MOS nanostructure-based H$_2$ sensors. Therefore, it is imperative to explore alternative approaches for enhancing sensor performance and minimizing energy consumption to align with the operational demands of the industry.

3.3. Modification of noble metal nanoparticles

The utilization of noble metal NPs (such as Pd,[71] Pt,[72] Au,[73,74] and Ag[75]) for the functionalization of MOSs represents an efficacious approach to augment the response and selectivity of resistive H_2 sensors based on MOSs. The modification of MOSs by noble metal NPs is predicated upon two fundamental mechanisms: chemical sensitization and electron sensitization, namely, the spillover effect and the Fermi-level control sensitization mechanism, respectively.[76,77]

Chemical sensitization is used to describe the process in which gas molecules are dissociated by metal NPs (e.g. Pd, Pt, and Au) and then spill over onto the surface of MOSs. Reducing the activation energy of the reaction effectively promotes the progress of the reaction without altering the intrinsic resistance of MOSs.[78] In particular, sometimes H_2 are dissociated into H^+ and electrons in the presence of catalysts, which are then intercalated into MOSs. This so-called "spillover" effect is well reported in MoO_3, WO_3, and V_2O_5.[79–82] Therefore, H_2 reactions on the surface of MOSs are effectively promoted by metal NPs, thereby enhancing H_2 sensing properties. On the other hand, electronic sensitization is generated through the electron interaction between metal NPs (e.g. Pd, Ag, and Cu) and the interface of MOSs. Upon exposure to air, the electronic sensitizers in the oxidized state act as strong acceptors of electrons that trap electrons from MOSs and generate a large amount of adsorbed oxygen on their surfaces, inducing a surface space charge layer which is strongly depletive of electrons in the MOSs near the interface.[78,83] However, when exposed to H_2, the electronic sensitizers are reduced back to their metallic states, causing relaxation of the space charge layer by giving electrons back to MOSs and resulting in a substantial resistance variation. The gas sensing performance of MOS-based sensors can be effectively enhanced by these two mechanisms involving metal NPs.

Among various noble metals, Pd and Pt are widely used as chemical sensitizers due to their excellent ability to induce the spillover effect of H_2 molecules onto MOSs for H_2 sensing. For instance, Cheng et al.[84] demonstrated that Pt decoration can greatly improve the ZnO sensor performance both in dry and humid environments due to the spillover effect, and Amit et al.[85] reported the significant contribution of Pd in augmenting the H_2 sensing performance of V_2O_5 through the spillover effect. In addition, Pd can also be used as an electronic sensitizer for MOS-based resistive H_2 gas sensors. In the presence of ambient air, oxygen adsorption on the surface of Pd leads to partial oxidation of metallic Pd into PdO. Consequently, the PdO as a potent electron acceptor induces an expanded surface space charge layer, resulting in electron depletion near the interface and giving rise to the formation of an electron depletion layer. In an H_2 environment, PdO is reduced back to Pd, releasing electrons that subsequently react with H_2 to form PdH_x. The combination of PdO, Pd or PdH_x with MOSs forms different heterojunctions that modulate electron transfer. For example, Meng et al.[83] observed that Pd existed in the forms of PdO, Pd, and PdH_x in different environments. Amongst others, PdO was a p-type semiconductor with a work function of 7.9 eV. Upon loading PdO onto the surface of n-type SnO_2, an electron transfer

occurred from SnO_2 to PdO due to the lower work function of SnO_2 (4.5 eV), resulting in the formation of a p–n heterojunction. Therefore, the working temperature decreased from 300 to 125 °C and the sensitivity remarkably upgraded after Pd loading in SnO_2. Furthermore, in most cases, there is a strong correlation between chemical sensitization and electronic sensitization, which synergistically enhances the gas sensing performance of MOSs. For instance, Liu et al.[86] fabricated a H_2 sensor based on Pd/SnO_2 and demonstrated the coexistence of both sensitization mechanisms in gas sensing reactions, which exhibited a pronounced dependence on the concentration of H_2. When the H_2 concentration was less than 1%, the electronic coupling effect at the PdH_x and SnO_2 interfaces became predominant (Fig. 6a). Upon a further increase in H_2 concentration, the main mechanism was the redox reaction between H_2 and $O^{\alpha-}$ on the surface of SnO_2 (Fig. 6a). The loading of Pd effectively reduced the activation energy of the reaction, which significantly improved the sensor's kinetic performance. Furthermore, a significant decrease in its sensitivity to additional disruptive gases was observed, indicating an elevated degree of selectivity (Fig. 6b). Therefore, diverse MOSs, including SnO_2,[87] ZnO,[84] In_2O_3,[73] TiO_2,[72,88] WO_3,[89] and V_2O_5,[85] functionalized by Pt, Pd, or Au, have been reported for selective H_2 sensing layers so far.

In particular, compared with widely used Pd NPs, bimetallic NPs demonstrate higher electro-catalytic characteristics due to their specific structure and the synergism of two components.[91] At present, the commonly used bimetallic catalysts are PdPt,[92] PdAu,[93] PdAg,[94] PtAu,[95,96] PtAg,[97] and AgAu[97] etc. For example, Meng et al.[45] proposed that $PdPt/SnO_2$ materials exhibited shape-dependent H_2 sensing performances due to the different morphologies of the PdPt sensitizer, such as nano-octahedrons, nanocubes and nanoflowers. Amongst others, the nano-octahedron modified SnO_2 (NOS) exhibited ultrahigh response (22821) and superfast response/recovery time (1/8 s) towards 1000 ppm H_2 at 25 °C, which was superior to the MOS-based H_2 sensing materials reported so far in terms of working temperature, response speed and response value (Fig. 6c–e). Kumar et al.[94] demonstrated that the sensor with a 1:1 Ag:Pd/ZnO has shown a high response of 51.36 towards 100 ppm of H_2 at an operating temperature of 275 °C. Consequently, the bimetallic NPs can efficiently increase the response value and decrease the operating temperature.

However, the decorated metal NPs on the surface of MOSs tend to undergo facile aggregation and delamination from the MOS-based materials.[98] In particular, the surfaces of metal NPs can be easily poisoned by many chemicals that contain sulfur (H_2S, SO_2, and thiols) or phosphorus.[99] Therefore, the metal@oxide core–shell nanostructures can overcome the above-mentioned drawbacks. In this context, core–shell sensing materials can offer a substantial increase in surface area, structural stability, enhanced activities, and synergistic properties.[100] For instance, Nguyen et al.[90] reported that PdPt@ZnO core–shell nanoparticles (CSNPs) exhibited impressive H_2 sensing performances. The results showed that the PdPt@ZnO sensor displayed a high response of 48 with respect to Pd@ZnO (22), Pt@ZnO (14), and free ZnO (9), along with fast response and recovery times (0.7 and 3 min) to 100 ppm H_2 at 350 °C. Here, the various core–shell sensors all exhibited a higher
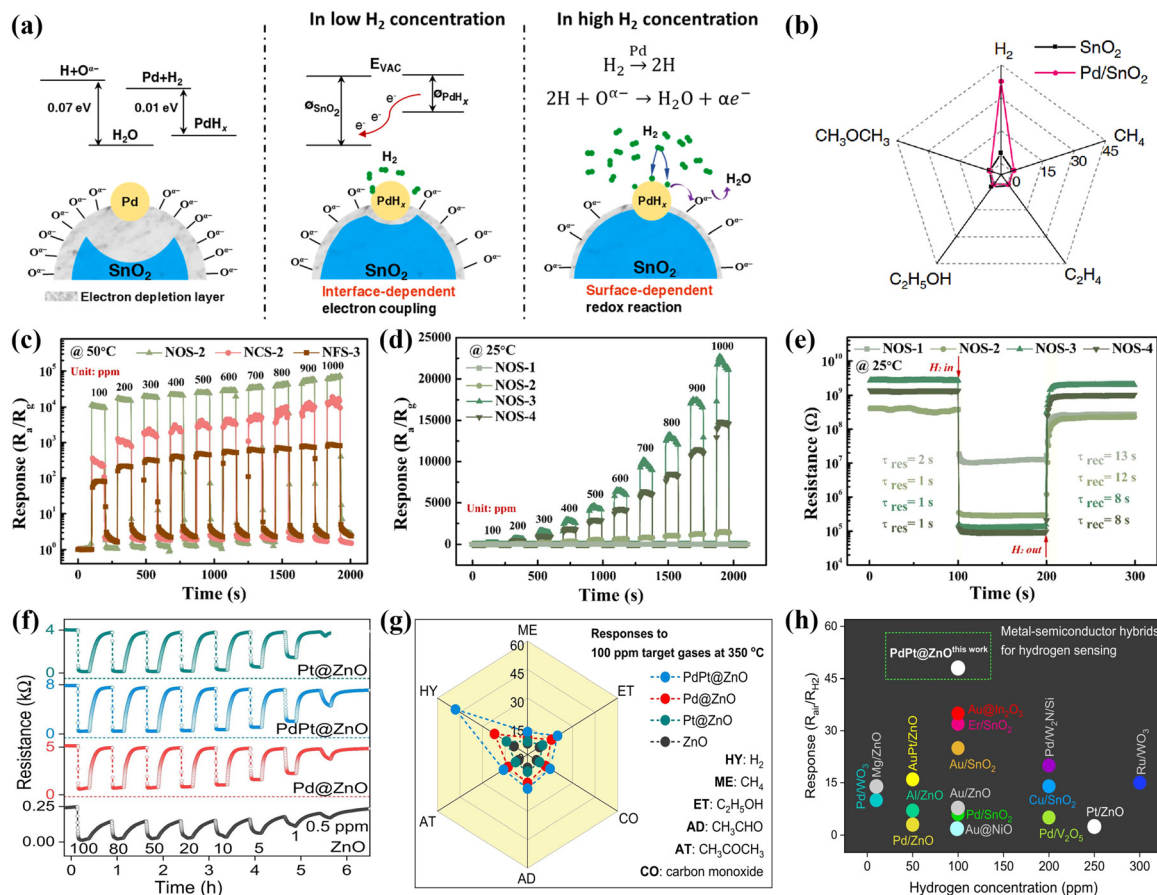
Fig. 6 (a) Schematic illustration of a model for the change in reception and transduction mechanisms for Pd/SnO$_2$ films. (b) Selectivity of SnO$_2$ and Pd/SnO$_2$ to H$_2$ in comparison with interfering gases including CH$_3$OCH$_3$, C$_2$H$_5$OH, C$_2$H$_4$ and CH$_4$. Reproduced with permission from ref. 86. Copyright 2024 Elsevier. (c) Response–recovery curves of NOS-2, NCS-2 and NFS-3 to different H$_2$ concentrations ranging from 100 to 1000 ppm at 50 °C. (d) Response–recovery curves for NOS-1, NOS-2, NOS-3 and NOS-4 of different H$_2$ concentrations from 100 to 1000 ppm at 25 °C. (e) Response/recovery times for NOS-1, NOS-2, NOS-3 and NOS-4 to 1000 ppm H$_2$ at 25 °C. Reproduced with permission from ref. 45. Copyright 2023 Elsevier. (f) The dynamic sensing responses of the pure ZnO, Pd@ZnO, PdPt@ZnO, and Pt@ZnO CSNP sensors of varied H$_2$ concentration from 0.5 to 100 ppm at 350 °C. (g) Selectivity of pure ZnO, Pd@ZnO, Pt@ZnO, and PdPt@ZnO sensors to 100 ppm H$_2$ at 350 °C in comparison with interfering gases including CH$_4$, C$_2$H$_5$OH, CH$_3$CHO, CH$_3$COCH$_3$, and CO. (h) A comparison with recently reported advanced sensors based on different types of single metal NP decorated MOSs in terms of H$_2$ sensing performance. Reproduced with permission from ref. 90. Copyright 2022 Elsevier.

response towards each of the tested target gases (especially towards H$_2$) compared to that of the pure ZnO (Fig. 6f and g). Further, the superiority of the PdPt@ZnO CSNPs over other previously reported devices for H$_2$ detection was indicated in Fig. 6h. The observed enhancements can be ascribed to several factors: (1) the exceptional catalytic activity of the alloyed PdPt core, (2) the abundant presence of oxygen vacancies and chemisorbed oxygen in the ZnO shell, (3) the facile two-way transfer of electrons between the core and shell, and (4) the substantial surface area and porosity exhibited by CSNPs. From this perspective, diverse core–shell nanostructures based on MOSs have been reported as highly sensitive and selective H$_2$ sensing layers.[90,101,102]

3.4. Doping of elements

Many investigations have indicated that doping of elements can significantly influence the morphology, crystal structure, adsorption capacity, and electrical properties of materials, thus serving as a prevalent strategy to enhance the gas-sensing

performance of MOSs. In particular, when elements enter the lattice of MOS as acceptor or donor impurities, they induce a shift in the Fermi level and consequently change the band structure.[103] For n-type semiconductors, the Fermi level shifts up after the introduction of the donor impurity (providing electrons), because the donor impurity can introduce a set of fully occupied energy levels in the forbidden band near the conduction band, known as the donor level. Electrons at this level can readily transition to the conduction band, facilitating electrical conductivity. For p-type semiconductors, upon introducing an acceptor impurity (providing holes), there is a downward movement of the Fermi level. This is because the acceptor impurity introduces a set of completely unoccupied energy levels within the forbidden band close to the valence band, referred to as the acceptor level. Electrons in the valence band can easily transition to this level, leaving behind holes that contribute to conductivity in the valence band. So far, numerous MOSs doped by various elements have

been developed, including SnO$_2$, Fe$_2$O$_3$, CuO, ZnO, and TiO.[104–109]

For example, Li *et al.*[105] employed the electrospinning and calcination technique to incorporate La^{3+} ions into SnO$_2$ nanofibers at varying atomic molar ratio (AMR) concerning Sn. They found that the introduction of La changes the grain size of SnO$_2$. The average grain sizes of SnO$_2$ nanofibers and La-doped SnO$_2$ nanofibers (Fig. 7a) were calculated to be 11.9 nm (AMR 0), 11.5 nm (AMR 0.5%), 11.4 nm (AMR 1%) and 11.7 nm (AMR 3%), respectively. And all the La-doped SnO$_2$ showed higher sensitivity than pristine SnO$_2$ due to the polaron effect induced by La, which can provide fast dissociative adsorption of H$_2$ on the surface (Fig. 7b). Among them, the sensor with 1% AMR exhibited the best H$_2$ sensing performance (Fig. 7b and c). In addition, Hsiao *et al.*[108] developed five different doping concentrations ranging from 0 to 4% W to the ZnO structure to find an appropriate doping concentration in H$_2$ sensing. As shown

in Fig. 7d, the grain structure was uniformly deposited on the surface (Fig. 7d(vi)), and with an increase in the doping concentration of W, the grain size of W-doped ZnO decreased correspondingly (Fig. 7d(i)–(v)) due to the smaller ionic radius of W (0.064 nm) compared to that of Zn (0.074 nm). Furthermore, the performance test results showed that the optimal doping concentration of W was 3% and the optimal working temperature was 150 °C (Fig. 7e). As depicted in Fig. 7f, the 3% W doped ZnO exhibited a high response of 67% for 100 ppm concentration of H$_2$ at 150 °C. Herein, W served as a catalyst for enhancing the adsorption of oxygen species on the surface of ZnO.

In addition to affecting the morphology of materials, doped elements can also reduce the charge carrier concentration and affect the thickness of the material space charge layer by causing hole electron recombination in MOSs, thus improving the sensor sensitivity.[110] For instance, Ai *et al.*[106] reported that
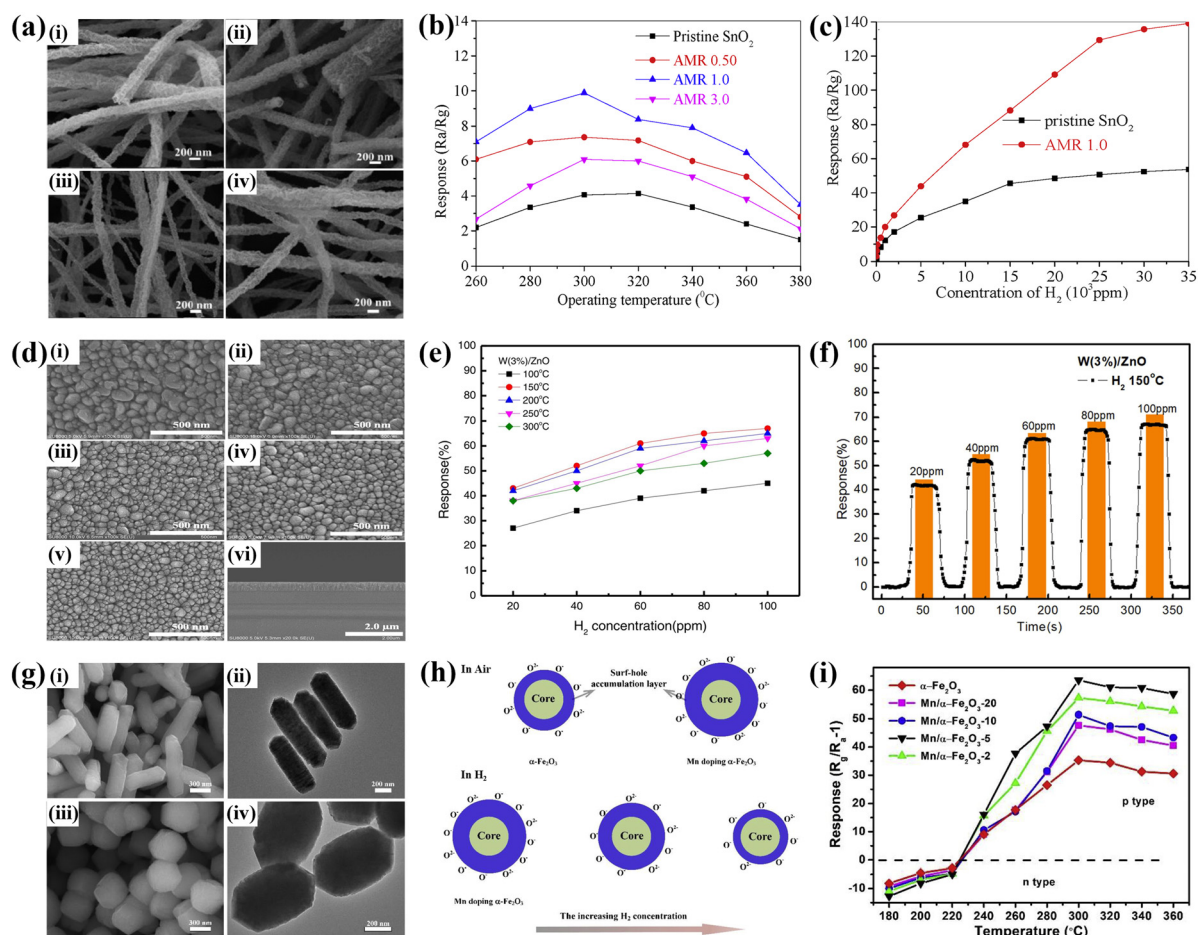
Fig. 7 (a) SEM images of the SnO$_2$ nanofibers with La doping concentrations at (i) 0%, (ii) 0.5%, (iii) 1%, and (iv) 3%. (b) Response of SnO$_2$ and La-doped SnO$_2$ nanofibers to 100 ppm H$_2$ at different operating temperatures. (c) Response of SnO$_2$ and 1% La-doped SnO$_2$ to different H$_2$ concentrations from 5 to 35 000 ppm. Reproduced with permission from ref. 105. Copyright 2019 Elsevier. (d) SEM images of ZnO with W doping concentrations at (i) 0%, (ii) 1%, (iii) 2%, (iv) 3%, and (v) 4%. (vi) Cross-sectional image of W(4%)/ZnO. (e) Response of W(3%)/ZnO to H$_2$ from 20 to 100 ppm at different temperatures. (f) Response–recovery curve of W(3%)/ZnO to different H$_2$ concentrations ranging from 20 to 100 ppm at 150 °C. Reproduced with permission from ref. 108. Copyright 2023 Elsevier. (g) SEM and TEM images of α-Fe$_2$O$_3$ and Mn/α-Fe$_2$O$_3$-5. (i) SEM image of α-Fe$_2$O$_3$, (ii) TEM image of α-Fe$_2$O$_3$, (iii) SEM image of Mn/α-Fe$_2$O$_3$-5, (iv) TEM image of Mn/α-Fe$_2$O$_3$-5. (h) Schematic diagram of the core/shell conductive structure of α-Fe$_2$O$_3$ and Mn doping of α-Fe$_2$O$_3$ in the air and Mn doping of α-Fe$_2$O$_3$ in different H$_2$ concentrations. (i) Response of α-Fe$_2$O$_3$, Mn/α-Fe$_2$O$_3$-20, Mn/α-Fe$_2$O$_3$-10, Mn/α-Fe$_2$O$_3$-5, and Mn/α-Fe$_2$O$_3$-2 to 200 ppm H$_2$ with different temperatures. Reproduced with permission from ref. 106. Copyright 2022 Elsevier.

Mn-doped α-Fe₂O₃ synthesized by the hydrothermal method in H₂ sensing. Herein, the morphology of α-Fe₂O₃ changed from rod to polyhedron by introducing Mn, as depicted in Fig. 7g. Furthermore, it was observed that the substitution of high-priced Fe ions with low-priced Mn ions led to the formation of a relatively high concentration of surface oxygen vacancy defects on the Mn/α-Fe₂O₃-x nanoparticles. Consequently, compared to α-Fe₂O₃, Mn/α-Fe₂O₃-x exhibited an increased adsorption capacity for oxygen ions (Fig. 7h). Upon exposure to H₂ gas, the trapped electrons were released into Mn/α-Fe₂O₃-x through the reaction between H₂ molecules and absorbed oxygen ions, resulting in a reduction in the thickness of the hole accumulation layer (Fig. 7h). Therefore, this change in carrier concentration caused by gas reactions resulted in a more significant alteration in sensor resistance and consequently enhanced gas response (Fig. 7i). Consequently, doping of elements can significantly improve the performance of MOS-based H₂ sensors in various aspects.

3.5. MOS-based composites

The incorporation of MOSs with other materials can improve the H₂ sensing properties due to their synergistic effect. The introduction of other materials into MOSs can lead to the formation of heterojunctions, which updates the charge distribution within the material and establishes a barrier at the material interface. This results in carrier depletion in one material and carrier accumulation in another, thereby significantly altering the total number of charge carriers present and enhancing both the sensitivity and selectivity of the sensor.[11,111,112]

Notably, the electronic properties of heterojunctions rely fundamentally on band alignment/bending and the accompanying charge transfer/separation. For semiconductor–semiconductor heterojunctions, three distinct types of band alignments exist, namely straddling (type I), staggered (type II), and broken gap (type III).[113] Regarding the type I band alignment, the conduction band minimum (CBM) and valence band maximum (VBM) of both semiconductor materials are straddled, making the two band edges of one material completely fall into another.[113] This results in the spontaneous transfer of electrons and holes from the large-bandgap material to the small-bandgap material, which improves the migration efficiency of charge carriers without providing additional energy, thereby

further enhancing the H₂ sensing performance (Fig. 8a). In the case of type II band alignment, there is a staggered arrangement of band edges between the two materials, resulting in only the CBM of one material falling within the bandgap of the other material.[113] Unlike type I band alignment, this alignment allows for effective spatial separation of holes and electrons as they are transferred to different materials, which significantly increases the concentration of charge carriers, thereby improving the sensitivity of H₂ sensors. The type III band alignment is characterized by a complete breaking of the band edges between the two materials, with the CBM of one material positioned lower than the VBM of the other material, indicating a partial overlap between their respective bands (Fig. 8c).[113] However, heterostructures with type III band characteristics are relatively rare due to the unique nature of band structures and there is no migration of electrons and holes between the two materials. Consequently, there are few research studies on hydrogen sensors based on type III heterojunctions.

To date, extensive reports have been published on the utilization of MOSs for forming heterojunctions to enhance the performance of H₂ sensors, including SnO₂/Sb₂O₃,[114] SnO₂/WO₃,[115] SnO₂/ZnO,[116] In₂O₃/ZnO,[117] and In₂O₃/SnO₂.[118] For example, Wang et al.[117] investigated the effect of In₂O₃ modified by ZnO with different weight percentages on H₂ sensing performance. As depicted in Fig. 9a, the ZnO synthesized by calcination of precursor ZIF-8 with a regular dodecahedral structure and the In₂O₃ exhibited two different crystal phases, namely cubic phase c-In₂O₃ (Inc) and hexagonal h-In₂O₃ (Inh). The H₂ sensing performance test results demonstrated that the ZnO (5%)-Inc/Inh-based sensor exhibited the highest sensitivity at 450 °C when ZnO constituted 5 wt% of In₂O₃ (Fig. 9b). Herein, the n-type In₂O₃ and n-type ZnO formed a type II heterojunction, as shown in 7c. When exposed to H₂, the adsorbed oxygen on the surface of ZnO (5%)-Inc/Inh reacted with H₂, resulting in the release of electrons that effectively reduced the potential barrier and significantly enhanced the conductivity of the sensitive layer. Furthermore, the performance advantages of ZnO-Inc/Inh were investigated using density functional theory. The response of the composite system consisting of c-In₂O₃ and h-In₂O₃ to H₂ was theoretically more pronounced compared to that of the single crystalline phase In₂O₃. In addition, the incorporation of ZnO results in
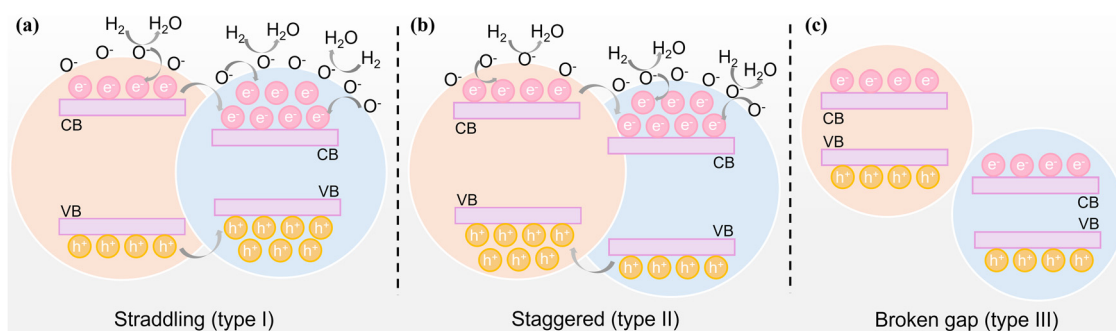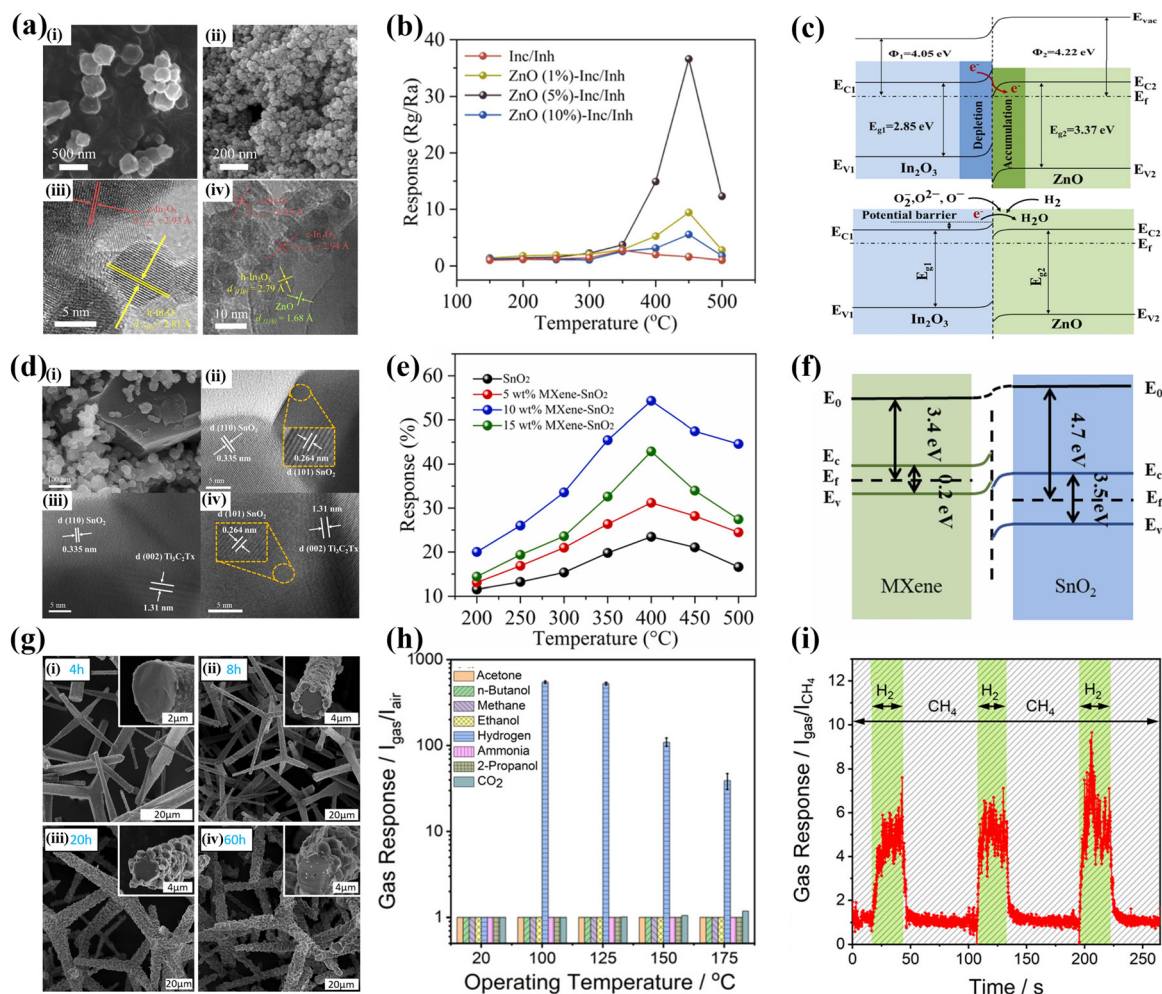

Fig. 8 Schematic of three types of heterojunctions. (a) Type of straddling. (b) Type of staggered. (c) Type of broken gap.

Fig. 9 (a) SEM images of (i) ZnO and (ii) Inc/Inh; HRTEM images of (iii) Inc/Inh and (iv) ZnO-Inc/Inh. (b) Response of Inc/Inh-based sensors to 2000 ppm H_2 at different operating temperatures ranging from 100 to 500 °C. (c) Sensing mechanism of the heterojunction between In_2O_3 and ZnO. Reproduced with permission from ref. 117. Copyright 2024 Elsevier. (d) (i) SEM image of 10 wt% MXene−SnO_2, (ii) HRTEM image of SnO_2, and (iii) and (iv) HRTEM image of 10 wt% MXene−SnO_2. (e) Response of SnO_2-based sensors to 600 ppm H_2 at different operating temperatures ranging from 200 to 500 °C. (f) Schematic diagram of the heterojunction between MXene and SnO_2. Reproduced with permission from ref. 119. Copyright 2024 Elsevier. (g) SEM images of t-ZnO@ZIF-8 at different reaction times of 4, 8, 20, and 60 h. (h) Selectivity of the t-ZnO@ZIF-8 (4 h)-based sensor to 100 ppm of different gases at different operating temperatures on $\log_{10}$ scales. (i) Response−recovery curve of t-ZnO@ZIF-8 (4 h) to 100 ppm H_2 in CH_4 at 100 °C. Reproduced with permission from ref. 120. Copyright 2023 American Chemical Society.

more pronounced charge transfer, variations in band gap, and alterations in the density of states in the composite, thereby indicating the presence of enhanced H_2 sensing performance.

In addition to MOS/MOS-based composites, the integration of MOSs with other materials can also give rise to heterojunctions, such as graphene,[121] MoS_2,[122] WS_2,[123] and MXene.[119] Recently, Chen et al.[119] compared the H_2 sensing performance of single SnO_2 and a MXene–SnO_2 composite. As illustrated in Fig. 9d, the connection between the hexagonal SnO_2 nanosheets and the MXene layered nanomaterial was well-established. Compared to the single SnO_2-based sensor, all the MXene–SnO_2-based sensors exhibited a significantly enhanced response to H_2. Notably, among them, the 10 wt% MXene–SnO_2-based sensor demonstrated the highest sensitivity at an optimal temperature of 400 °C (Fig. 9e). Herein, the p-type MXene and the n-type SnO_2 participated in the formation of p–n heterostructures in the

composite (Fig. 9f), which enhanced the H_2 sensing properties due to the strong interaction formed by the surface adsorption of the H_2 molecular heterojunction interface.

Moreover, the incorporation of MOFs with MOSs is commonly employed to enhance selectivity owing to their tunable pore sizes, which enables them to function as molecular sieves.[120,124,125] For instance, Poschmann et al.[120] reported a ZIF-8 functionalized single-crystalline tetrapodal ZnO gas sensor, which can detect H_2 in CH_4. Amongst others, the formation of ZIF-8 was achieved through the reaction between ZnO tetrapods (t-ZnO) and evaporating 2-methylimidazole (HMeIM), followed by gas-phase crystallization to obtain t-ZnO@ZIF-8. As shown in Fig. 9g, the amount of ZIF-8 formed and the thickness of the ZIF-8 coating were significantly influenced by the reaction time, with a higher conversion of t-ZnO into ZIF-8 for observed longer reaction times. Among them, the t-ZnO@ZIF-8 (4 h) sample was

selected for gas sensing behavior study due to the decrease in surface area of tetrapod arm ends with increased reaction time, making electrical contact more challenging; additionally, thin MOF coatings can result in faster response/recovery speed. As depicted in Fig. 9h, the t-ZnO@ZIF-8 (4 h)-based sensor had no response for all tested gases at room temperature; however, with the operating temperature increasing, it exhibited extremely high response to H_2 with a high selectivity. The exceptional sensing performance can be summarized as follows: (1) ZIF-8 acted as a molecular sieve, enhancing the selectivity and sensitivity of t-ZnO to H_2; (2) the formation of ZIF-8 introduced defects at the interface with t-ZnO, enabling modulation of the resistance of single crystalline ZnO by H_2 in the absence of atmospheric O_2. Furthermore, they tested the response of a t-ZnO@ZIF-8 (4 h)-based sensor to 100 ppm H_2 in CH_4. However, the presence of CH_4 did not affect the fast response to H_2 of the sensor. Therefore, it should also be feasible to quantify the concentration ratio of an H_2/CH_4 mixture, rendering it a promising sensor for H_2 detection in natural gas pipelines. From this perspective, the introduction of selective sieving layers on MOSs is one of the most promising strategies to attain enhanced selectivity towards H_2.

To date, the performance of MOS-based H_2 sensors has been significantly enhanced through various improvement methods. Table 2 summarizes the sensing characteristics of recently reported MOS-based H_2 sensors. The response values, response/recovery times, selectivity, long-term stability, and detection limits of a few sensors have been demonstrated to be exceptional at room temperature. However, the practical applications of the majority of sensors are still hindered by their requirement for operation at high temperatures. At elevated operating temperatures, other gas molecules are also able to react with MOSs, leading to resistance changes and consequently compromising the selectivity of MOS-based sensors. Additionally, prolonged exposure to high temperatures can adversely impact the long-term stability of sensors by diminishing their sensitivity and shortening their lifespan. Furthermore, MOS-based sensors are also prone to the influence of H_2O molecules in the surrounding environment. Hence, operating at near room temperature and exhibiting excellent humidity resistance in practical applications are essential for MOS-based H_2 sensors.

4. Others

4.1. Graphene

Graphene has gathered significant interest as a sensing material owing to its large specific surface area, high carrier mobility, high conductivity, and excellent physical and chemical properties.[126] It has been demonstrated that the gas sensing mechanism based on graphene heavily relies on physisorption.[127] Physisorption refers to the absorption of gas molecules onto the surface of sensing materials through intermolecular forces (van der Waals force) without forming chemical bonds, and the corresponding charge

Table 2 Summary of sensing properties of MOS-based H_2 sensors

Material	Morphology	Conc. (ppm)	Tem. ($^\circ$C)	Res.	T_{res}/T_{rec} (s)	MDL (ppm)	Ref.
SnO_2	Nanowires	150	250	54[a]	19/45	0.5	66
ZnO	Nanorods	80	180	483%[b]	15.1/100.1	0.5	67
Sn_3O_4	Nanosheets	10	150	2.2[a]	9.4/24	0.05	69
ZnO	Hollow hexahedron	300	250	101%[b]	611/1137	5	75
Pd/SnO_2	Nanowires	40	150	8.5[a]	6/3	—	66
Pd/CeO_2	Hollow strings	10 000	RT	2.68%[b]	10/—	100	71
Pd/SnO_2	Nanoparticles	500	125	254[a]	1/22	10	83
Ag/ZnO	Hollow hexahedron	300	250	479%[b]	175/655	5	75
Pt/TiO_2	Nanorods	1	RT	1.21[a]	42/30	1	88
Pd/WO_3	Nanoflowers	500	150	8658.98[a]	1/3	20	89
$Pd–Au/In_2O_3$	Nanocubes	500	250	55[a]	5/3	0.3	73
$PdPt@In_2O_3$	Spheres	100	RT	29.8[a]	58/200	5	102
Ag–Pd/ZnO	Nanorods	100	275	51.36[a]	—	—	94
PdPt@ZnO	Nanoparticles	100	350	48[a]	0.7/180	0.5	90
$Pd–Au@SnO_2$	Nanorods	100	175	46.4[a]	19/302	25	93
$Au@Pd/SnO_2$	Nanospheres	100	100	16.75[a]	1/5	10	91
$PdPt/SnO_2$	Nano-octahedrons	1000	RT	22821[a]	1/8	100	45
$Mn/\alpha-Fe_2O_3$	Polyhedrons	200	300	63.5[a]	10/24	10	106
Cu/TiO_2	Films	1000	200	2284%[c]	128/129	—	109
W/ZnO	Films	100	150	67%[b]	—	20	108
Cu/SnO_2	Multilayer 3D	100	180	45%[b]	18/84	20	110
In_2O_3/SnO_2	Nanofibers	50	350	3.5[a]	1.1/1.9	50	118
SnO_2/WO_3	Spheres/plates	500	150	91%[b]	35/269	10	115
In_2O_3/ZnO	Nanoparticles/dodecahedrons	5000	450	79.91[a]	1/6	0.053	117
SnO_2/ZnO	Films	30	200	93[a]	50/29	0.25	116
$Pd–WO_3/WS_2$	Nanoflowers	1000	125	4227.35[a]	1/25	20	123
$SnO_2/MXene$	Nanosheets	500	400	76%[b]	13/15	10	119
ZnO@ZIF-8	Tetrapods	100	100	546[d]	2/2	5	120

Conc.: gas concentration; Tem.: operating temperature of the sensor; RT: room temperature ($\sim$25 $^\circ$C); Res.: response of the sensor. [a] Response is defined as R_{gas}/R_{air}. [b] Response is defined as $(R_{gas} - R_{air})/R_{air} \times 100\%$. [c] Response is defined as $(I_{gas} - I_{air})/I_{air} \times 100\%$. [d] response is defined as I_{gas}/I_{air}; T_{res}: response time of the sensor; T_{rec}: recovery time of the sensor; MDL: minimum detection limit of the sensor; Ref.: reference; —: not reported; 3D: three-dimensional.

transfer mechanism does not rely on the breakdown of the absorbed gas. Gas molecules absorb on the surface of graphene and act as electron donors or acceptors.[127] Herein, H_2 molecules serve as electron donors (Fig. 1c). It is worth noting that this absorption process can occur at low temperatures and in the absence of oxygen. However, it always requires the sensing material with a favorable surface adsorption energy value for the target gas molecules and optimal electronic band structure facilitating the charge transfer.[128] Additionally, physisorption exhibits some problems including poor reversibility and weak response magnitude. Based on these results, bare graphene is not great for H_2 sensing, so the introduction of catalysts to enhance the H_2 adsorption was crucially important.

So far, many H_2 sensors based on catalyst-functionalized graphene have been reported.[129–132] For instance, Zhu et al.[129] designed a flexible H_2 sensing film based on Pd nanoclusters/reduced graphene oxide (rGO) via one-step vacuum filtration.

Amongst others, the rGO/Pd film sensor demonstrated superior response, rapid response/recovery kinetics, and exceptional stability in comparison to the bare rGO film due to the pronounced catalytic effect of ultrasmall (3.3 nm) Pd nanoclusters. Besides, the rGO/Pd-based flexible film sensor achieved a stable response to 2% H_2 after different bending states and still maintained excellent sensing performance after suffering from repeated bending/recovery deformations (Fig. 10a–c).

However, limited research has been conducted on enhancing the sensing performance through structural modifications of graphene. According to some reports, graphene obtained through exfoliation and chemical vapor deposition (CVD) exhibits chemical inertness due to the absence of dangling bonds,[135] while the nanocomposites based on 2D graphene tend to aggregate owing to π–π stacking and van der Waals forces acting between the layers of graphene.[131,136,137] These will all lead to the degradation of the H_2 sensing properties.
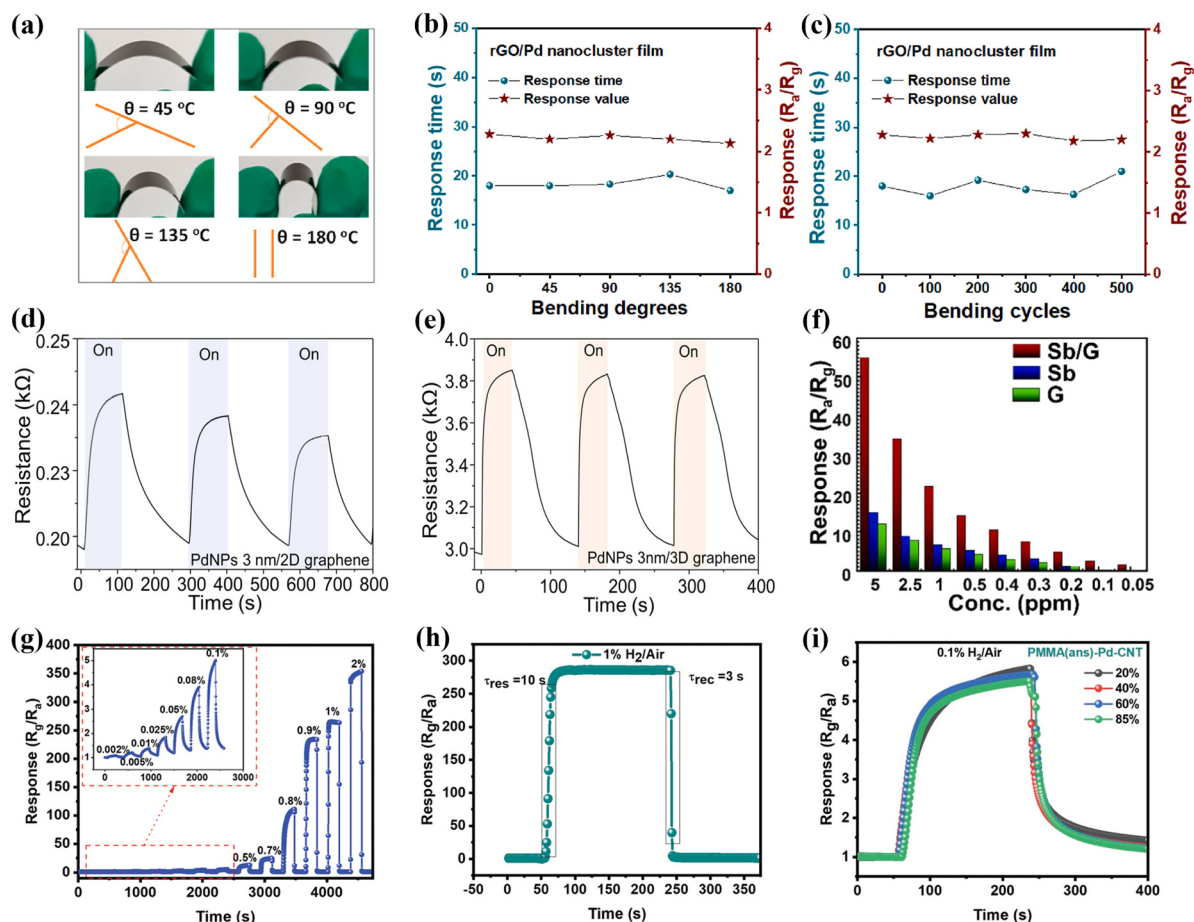
Fig. 10 (a) Photos of the rGO/Pd film at different bending degrees. (b) Response value and response time of the rGO/Pd-based sensor to 2% H_2 under different bending degrees at room temperature. (c) Response value and response time of the rGO/Pd-based sensor to 2% H_2 at room temperature after different bending cycles (one cycle: from 0° to 180° and back to 0°). Reproduced with permission from ref. 129. Copyright 2022 Elsevier. (d) Response–recovery curves of PdNPs (3 nm, the thickness of Pd layer)/2D graphene and (e) PdNPs (3 nm)/3D graphene to 3% H_2 at 30 °C. Reproduced with permission from ref. 131. Copyright 2024 Elsevier. (f) Response of G, Sb, and Sb/G-based sensors to different H_2 concentrations ranging from 0.05–5 ppm at room temperature. Reproduced with permission from ref. 133. Copyright 2024 Elsevier. (g) The response–recovery curve of the PMMA-Pd-SWNT sensor to different H_2 concentrations ranging from 0.002–2% at room temperature. (h) Response/recovery time of the PMMA-Pd-SWNT sensor to 1% H_2 at room temperature. (i) Response–recovery curves of the PMMA-Pd-SWNT sensor for different humidity to 0.1% H_2 at room temperature. Reproduced with permission from ref. 134. Copyright 2023 Wiley-VCH GmbH.

Thus, to take full advantage of graphene, it is important to modify the intrinsic 2D structure of graphene. Recently, Lee et al.[131] developed an H_2 sensor based on Pd-decorated 3D graphene, which was fabricated by introducing Cu vapor as the remote catalyst in a metal–organic CVD system to directly grow 3D graphene on 300 nm SiO_2/Si substrates and decorating with thermally evaporated Pd NPs. As shown in Fig. 10d and e, when the same thickness of Pd NPs were deposited on 2D and 3D graphene, the 3D graphene demonstrated a higher response of 41.9% towards 3% H_2 at 30 °C because of the larger surface area and dense distribution of Pd NPs on 3D graphene than those of 2D graphene. Therefore, this study provides a new idea for the improvement of the H_2 sensing properties.

On the other hand, the heterostructures of graphene-based composites also display interesting H_2 sensing characteristics. In the heterostructures, graphene serves as a versatile platform, which not only possesses a huge specific surface area but also provides a highly conductive path for charge transport upon gas adsorption and desorption. For example, Kumar et al.[133] fabricated a class of heterostructures based on 2D Pnictogens and graphene by photolithography and pattern transfer methods for H_2 detection at room temperature. Amongst the Pnictogen class, antimonene/graphene (Sb/G) showed excellent H_2 sensing properties. As depicted in Fig. 10f, the Sb/G heterostructure displayed a superior response of 54.5 towards 5 ppm H_2 as compared to individual Sb (15.3) and G (12.1). Besides, it also showed short response/recovery time (12/34 s), low detection limit (50 ppb), high selectivity, and long-term stability. In a nutshell, the extraordinary H_2 sensing behavior can be ascribed to the heterostructure and electronic states, which provided a large density of active pathways, a high surface-to-volume ratio, and a tunable Schottky barrier. Thus, it provides the possibility to expand a novel family of Pnictogen-graphene sensors.

4.2. CNTs

CNTs have been investigated for real-time detection of gases at room temperature due to their high-quality crystal lattices, tunable electrical properties, and chemical sensitivity.[138,139] However, similar to graphene, the bare CNTs have no appreciable interaction with H_2, thus necessitating the exploration of suitable H_2 sensitive materials for CNTs functionalization.[140] To date, Pd is the most commonly employed catalyst for H_2 sensing due to its superior selectivity in absorbing H_2, while conducting polymers are commonly used as molecular sieves.[134,141–144] Moreover, there are also reports available based on Pt/CNTs.[145,146] Typically, CNTs are employed to enhance the conductivity of the composites, thereby improving the efficiency of electron transport and aggregation. Additionally, they act as supporting frameworks for increasing the surface-to-volume ratio, providing more active sites and consequently enhancing the absorption of H_2.[147]

Recently, Du et al.[141] constructed nanoarchitectures of Pd and poly-3, 4-ethylenedioxythiophene (PEDOT) coatings on multi-walled CNTs, which achieved dual H_2 and NH_3 detection. Herein, the multi-walled CNTs were used for both improving the surface ratio and assisting electron transfer. Notably, the PEDOT@CNTs exhibited negligible sensitivity to H_2, indicating that the presence of PEDOT wrapping on the CNTs did not directly influence H_2 sensing. Instead, the H_2 sensing capability of Pd&PEDOT@CNTs was primarily governed by the Pd NPs. Furthermore, it was also observed that the size distribution of the Pd NP coating on the CNTs also affected the H_2 sensing characteristics. In another case, Girma et al.[134] successfully fabricated reproducible and highly sensitive semiconducting single-walled carbon nanotube (SWNT) sensors by coating PMMA and decorating Pd. The uniform-density and monolayer SWNT films were synthesized using chemical immobilization through the click reaction between azide-functionalized polymer-wrapped SWNTs and immobilized alkyne polymer on a substrate before decorating with Pd nanoparticles (0.5–3.0 nm). As illustrated in Fig. 10g and h, the PMMA-Pd-SWNT sensor demonstrated a wide detection range of H_2 concentrations (0.002–2%) and a high response up to 285 at 1% H_2 with the response/recovery time of 10/3 s at room temperature. Amongst others, Pd efficiently reduced the activation energy of the surface reactions and enhanced the adsorption of H_2 and desorption of H_2O molecules, while the PMMA layer greatly optimized the film morphology and reduced the apparent activation energy, contributing to a high response and a fast response/recovery speed. Furthermore, the introduction of the PMMA layer effectively prevented H_2O molecules from diffusing and allowed H_2 permeation, which guaranteed stable operation at high humidity of the PMMA-Pd-SWNT sensor (Fig. 10i).

In addition to catalyst type and size distribution, the band gap of CNTs also exerts an influence on H_2 sensing performance. The difference in the band gap of CNTs will restrict the transition of electrons from the valence to the conduction band, resulting in an unequal number of holes in the valence band. For example, Zhang et al.[144] explored the effect of the diameters of SWNTs on H_2 detection. The results demonstrated that the response of the sensor with 0.7–1.2 nm SWNTs to 1 ppm H_2 was approximately 6 times compared to that of the one with 1.2–1.6 nm. That was because the wider band gap of 0.7–1.2 nm p-type SWNTs resulted in fewer holes in the valence band and easier depletion of holes by electrons from the dissociation of H_2. Therefore, researchers can optimize the performance of CNT-based H_2 sensors from multiple perspectives, including type of catalysts, size distribution of catalysts, and band gap of CNTs.

4.3. TMDs

Recently, 2D TMDs have demonstrated great potential for gas detection at room temperature due to their high surface-to-volume ratio, high carrier mobility, and tunable electrical and chemical properties.[148,149] To date, numerous studies have demonstrated the physisorption of H_2 on the surface of TMDs at room temperature.[128,150,151] However, TMDs always display relatively lower adsorption energy compared to other gases (such as NO_2, NO, CO, NH_3, CH_4, CO_2),[128,151] which is not conducive to developing highly sensitive and selective H_2 sensors based on pure TMDs. Therefore, extensive investigations have been conducted to address this issue by researchers.

So far, many literatures have suggested that it is efficient to improve the TMD-based H_2 sensing properties by combining catalysts with TMDs.[152–154]

For instance, Jiaswal *et al.*[153] reported a highly sensitive and selective H_2 sensor based on Pd NP-functionalized MoS_2 thin films. They prepared Pd/MoS_2 thin films *via* a single-step DC magnetron sputtering technique. As illustrated in Fig. 11a–c, compared to the pristine MoS_2 sensor, the Pd/MoS_2 sensor exhibited significantly enhanced H_2 sensing characteristics, including a high response of 33.7%, fast response/recovery time of 16/38 s to 500 ppm H_2 at room temperature, low detection limit of 1 ppm, and high H_2 selectivity against NH_3,
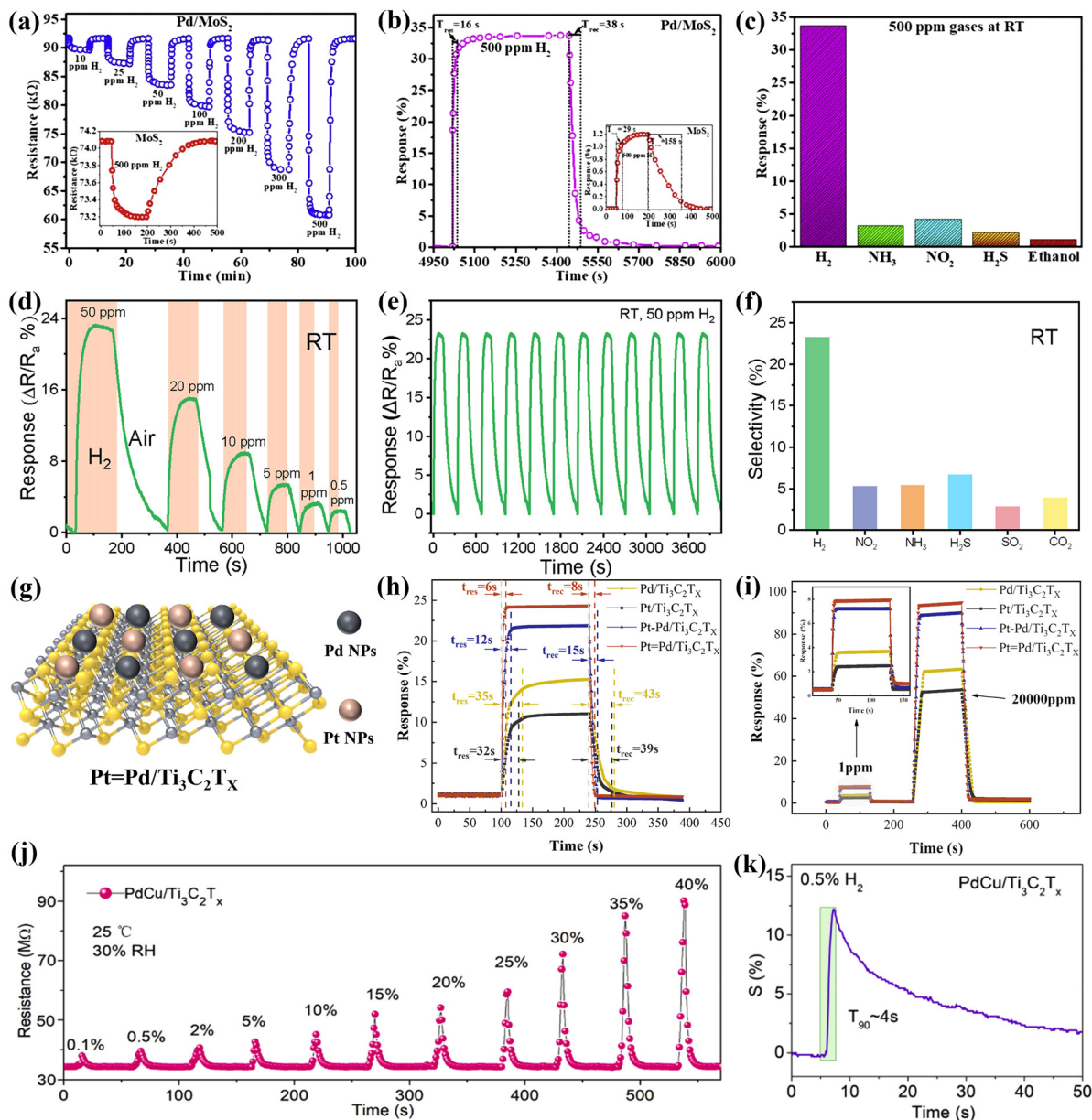
Fig. 11 (a) Response–recovery curve of Pd/MoS_2 to different H_2 concentrations ranging from 10–500 ppm at room temperature; the inset shows a response–recovery curve of Pd/MoS_2 to 500 ppm H_2 at room temperature. (b) Response/recovery times of Pd/MoS_2 and MoS_2 to 500 ppm H_2 at room temperature. (c) Selectivity of Pd/MoS_2 to 500 ppm H_2 in comparison with interfering gases including NH_3, NO_2, H_2S, and ethanol at room temperature. Reproduced with permission from ref. 153. Copyright 2020 Elsevier. (d) The response–recovery curve of Pt@MoS_2 to different H_2 concentrations ranging from 0.5–50 ppm. (e) Repeatability of Pt@MoS_2 to 50 ppm H_2 at room temperature. (f) Selectivity of Pt@MoS_2 to 50 ppm H_2 in comparison with interfering gases including NO_2, NH_3, H_2S, SO_2, and CO_2 at room temperature. Reproduced with permission from ref. 154. Copyright 2023 American Chemical Society. (g) Structure diagram of Pt = Pd/$Ti_3C_2T_x$. (h) Response/recovery times of $Ti_3C_2T_x$-based sensors to 200 ppm H_2 at room temperature; Pt–Pd represents an alloy of Pt and Pd. (i) Response–recovery curves of $Ti_3C_2T_x$-based sensors to 1 ppm and 20 000 ppm H_2. Reproduced with permission from ref. 155. Copyright 2023 Elsevier. (j) Response–recovery curves of PdCu and PdCu/$Ti_3C_2T_x$ to different H_2 concentrations ranging from 0.5–4% at 25 °C. (k) Response–recovery curve of PdCu/$Ti_3C_2T_x$ nanocomposites to different H_2 concentrations ranging from 0.1–40% at 25 °C. Reproduced with permission from ref. 156. Copyright 2024 Elsevier.

NO_2, H_2S, and ethanol. Therefore, the introduction of Pd NPs improved the sensing performance of MoS_2 owing to the catalytic activity of Pd and the creation of the Schottky barrier at the junction between Pd NPs and the MoS_2 semiconductor.

In addition to incorporating Pd NPs, Pt NPs were also integrated into 2D TMDs for the advancement of H_2 sensors. Wadhwa et al.[154] developed vertically aligned large-area MoS_2 flakes with enhanced H_2 sensing characteristics modified by Pt NPs. The presence of Pt NPs offered a surface reaction between H atoms and MoS_2 and supported the diffusion of H atoms into MoS_2. As depicted in Fig. 11d, the Pt@MoS_2-based sensor showed a high response of 23.2% to 50 ppm H_2 and an ultra-low detection limit of 0.5 ppm at room temperature, whereas the pristine MoS_2 only had a response of 9%. Besides, it displayed excellent repeatability and high selectivity (Fig. 11e and f). Therefore, it is imperative to modify TMDs with sensitizers, to develop TMD-based H_2 sensors with high sensing properties.

4.4. MXenes

MXenes represent a class of ternary, layered, machinable transition metal carbide, nitride and carbon nitride two-dimensional materials, and their chemical formula is $M_{n+1}AX_n$, where n = 1, 2, or 3, "M" is an early transition metal, "A" is a group of A (mostly groups 13 and 14), and "X" is the C element or N element.[157] In particular, MXenes exhibit a narrow band gap, a large specific surface area, an abundance of surface functional groups, and a high electron transfer rate,[157] rendering them highly suitable for applications in the field of H_2 detection. Herein, the sensing mechanisms for MXenes are similar to the above-mentioned MOS-based H_2 sensors.

Charan et al.[158] synthesized Ti_3C_2 nanosheets by selective etching of the Al layer from a prefabricated MAX phase (Ti_3AlC_2) precursor using hydrofluoric (HF) acid, which demonstrated a response of 1.24 with a response/recovery time of 32/125 s to 3000 ppm H_2 at room temperature. However, the pure MXene-based H_2 sensors usually present certain challenges including long response time, poor repeatability, and baseline drift.[119,158] Therefore, researchers have tried to employ metal NPs for the functionalization of MXenes or combine MXenes with other materials to augment their H_2 sensing properties.[155,156,159,160] For instance, Wang et al.[155] prepared spatially separated Pt and Pd modified $Ti_3C_2T_x$ (Pt = Pd/$Ti_3C_2T_x$, Fig. 10g) by a hydrothermal chemical reduction, which displayed excellent sensing performance at room temperature. A comparison of H_2 sensing performance between four different $Ti_3C_2T_x$-based sensors modified by Pt, Pd, Pt–Pd alloy, and Pt = Pd respectively was shown in Fig. 11h and i. All of them exhibited high responses to different H_2 concentrations at room temperature, whereas the pure $Ti_3C_2T_x$-based sensor almost had no response to H_2. Among them, the Pt = Pd/$Ti_3C_2T_x$-based sensor demonstrated the best sensing performance including the highest response value (24.6%) and the shortest response/recovery time (6/8 s) to 200 ppm H_2. Besides, it also exhibited an ultra-low limit of detection of 1 ppm (Fig. 11i), good repeatability, long-term stability, and high selectivity. Herein, Pt can enhance the dispersion of the Pt = Pd owing to the strong metal–support interaction (SMSI) effect and Pd had high adsorption and dissociation activity for H_2, so compared to monometallic-modified $Ti_3C_2T_x$ the Pt = Pd/$Ti_3C_2T_x$ showed superior H_2 sensing performances. Additionally, the higher H_2 sensing capabilities of Pt = Pd/$Ti_3C_2T_x$ than Pt–Pd/$Ti_3C_2T_x$ can be ascribed to the alloy formation of Pt–Pd weakening the electron transfer.

In addition, Qiu et al.[156] reported a 3D PdCu-modified $Ti_3C_2T_x$ nanocomposite prepared by a self-sacrificing template method. As depicted in Fig. 11j, compared to PdCu NPs, the PdCu/$Ti_3C_2T_x$ nanocomposites showed superior H_2 sensing behavior. Notably, the PdCu/$Ti_3C_2T_x$ nanocomposites exhibited consistent and stable response and recovery behaviors when exposed to a wide range of H_2 concentrations from 0.1 to 40% (Fig. 11k). Herein, the synergistic interaction and the heterostructure between PdCu NPs and $Ti_3C_2T_x$ resulted in the outstanding sensing performance of the PdCu/$Ti_3C_2T_x$ nanocomposites. Based on these findings, the utilization of metal NPs for the functionalization of MXenes and their integration with other materials have demonstrated remarkable efficacy in enhancing their hydrogen sensing capabilities.

So far, emerging materials, including graphene, CNTs, TMDs, and MXens, have exhibited some advancements in the realm of H_2 sensing. Table 3 summarizes the sensing performance of these materials in recent years. The sensing performance of these

Table 3 Summary of the sensing properties of other H_2 sensors

Material	Conc.	Tem. (°C)	Res.	T_{res}/T_{rec} (s)	MDL (ppm)	Ref.
rGO/Pd	2%	RT	2.28[a]	18/—	2500	129
Pd-GO	35 ppm	100	2.1%[b]	18/20	—	130
Sb/G	5 ppm	RT	54.5[a]	12/34	0.05	133
PMMA-Pd-SWNT	1%	RT	285[c]	10/3	20	134
Pd/HKUST-1/SWNT	1 ppm	RT	6.09[c]	—/1	1	144
Pt/MoS_2	1%	RT	8.7%[b]	8.1/16	500	152
Pd/MoS_2	500 ppm	RT	33.7%[b]	16/38	10	153
Pt/MoS_2	50 ppm	RT	23.2%[b]	33/121	0.5	154
Ti_3C_2	3000 ppm	RT	1.24[a]	32/125	500	158
PdCu/$Ti_3C_2T_x$	2%	RT	20%[b]	4/35	1000	156
Pt = Pd/$Ti_3C_2T_x$	200 ppm	RT	24.6%[b]	6/8	1	155

Conc.: gas concentration; Tem.: operating temperature of the sensor; RT: room temperature ($\sim$25 °C); Res.: response of the sensor. [a] Response is defined as R_{air}/R_{gas}. [b] Response is defined as $(R_{gas} - R_{air})/R_{air} \times 100\%$. [c] Response is defined as R_{gas}/R_{air}; T_{res}: response time of the sensor; T_{rec}: recovery time of the sensor; MDL: minimum detection limit of the sensor; Ref.: reference; —: not reported; HKUST-1: MOF copper(II) benzene-1,3,5-tricarboxylate.

Table 4 Summary of the advantages and disadvantages of each kind of material for chemiresistive H_2 sensors

Material	Advantages	Disadvantages
Pd-based	High selectivity Operating at room temperature	Poor long-term stability to high concentrations of H_2 Long response/recovery time High cost
MOS-based	High sensitivity Low detection limit Rapid response/recovery time	High operating temperature Poor selectivity Susceptible to humidity
Graphene	Operating at room temperature Large specific surface area High carrier mobility	Poor selectivity Long response/recovery time Low sensitivity
CNTs	Operating at room temperature High conductivity High surface-to-volume ratio	Poor reproducibility Low selectivity
TMDs	Operating at room temperature Tunable band gap	Poor selectivity Long response/recovery time
MXene	Operating at room temperature Large specific surface area	Poor sensitivity to low concentrations of H_2 Susceptible to humidity and oxygen

materials is highly efficient at room temperature; however, certain challenges persist. Graphene and CNTs exhibit low selectivity towards polar molecules and poor reproducibility. TMD-based H_2 sensors demonstrate prolonged response/recovery times, susceptibility to oxygen interference in ambient air, and high reactivity towards polar gases. Additionally, MXenes display inadequate sensing performance for low concentrations of H_2.

5. Conclusion and outlook

With the widespread application of hydrogen energy sources in various fields, there is a growing demand for high-performance chemiresistive H_2 sensors. In this review, we present a comprehensive overview of the recent advancements in chemiresistive H_2 sensors and provide a summary of the strategies employed for enhancing performance. For Pd-based sensors, the suppression of the phase transition and improvement in selectivity can be achieved through various approaches, encompassing nanostructure construction, device optimization, bimetallic formation, and integration with other materials. In the case of MOS-based sensors, enhancement of performance and reduction in operating temperature are attained *via* nanostructure design, surface modification, doping, and heterostructure construction. Regarding materials like graphene, CNTs, TMDs, and MXenes that are not inherently sensitive to H_2 themselves; their H_2 sensing primarily relies on the incorporation of Pd. In conclusion, we primarily discuss their enhancement mechanisms based on some representative research achievements in recent years.

Table 4 summarizes the advantages and disadvantages of each material. Despite significant advancements in the research of resistive H_2 sensors, there still exist certain challenges that necessitate further enhancements:

(1) Accurate measurement in different environments: the response signals of most sensors can be influenced by temperature and humidity, thereby constraining the reliability of practical applications for H_2 sensors. Furthermore, it is imperative to mitigate the influence of interfering gases in practical applications to achieve precise detection of the target gas. Hence, it is necessary to avoid cross-response and prevent false alarms.

(2) Achieving room temperature detection: most MOS-based H_2 sensors still operate at elevated temperatures, which not only improves their power consumption but also shortens their lifespan. Therefore, achieving room temperature operation is of great significance in reducing costs and improving safety in practical applications.

(3) Improving long-term stability: the poor long-term stability remains a significant challenge for most sensors in practical applications, particularly for Pd-based sensors, where achieving linear detection of high concentration H_2 while maintaining exceptional long-term stability proves to be arduous.

(4) Exploring novel materials: currently, the development based on Pd and MOS has gradually reached a state of maturity. Hence, it holds immense significance to explore novel materials capable of attaining heightened sensitivity, rapid response, superior selectivity, excellent humidity resistance, and operation at room temperature.

(5) Integration and miniaturization: with the advancement of the Internet of Things, the application scenarios for hydrogen gas sensors are progressively expanding. The integration of multiple functionalities into a compact sensor facilitates meeting diverse requirements across various scenarios.

Author contributions

Yao Yang Liu: writing original draft, collecting references. Zhong Li: writing review & editing, supervision, funding acquisition. Yi Liang: writing review & editing. Tao Tang: writing review & editing. Jing Hao Zhuang: collecting references. Wen Ji Zhang: collecting references. Bao Yue Zhang: writing review & editing. Jian Zhen Ou: writing review & editing, project administration, supervision.

Data availability

No primary research results, software or code and no new date were generated or analyzed as part of this review.

Conflicts of interest

There are no conflicts to declare.

Acknowledgements

References

1 H. S. Lee, J. Kim, H. Moon and W. Lee, *Adv. Mater.*, 2021, **33**, 2005929.
2 T. Hübert, L. Boon-Brett, G. Black and U. Banach, *Sens. Actuators, B*, 2011, **157**, 329–352.
3 B. Jang, W. Kim, M.-J. Song and W. Lee, *Sens. Actuators, B*, 2017, **240**, 186–192.
4 T. Sahoo and P. Kale, *Adv. Mater. Interfaces*, 2021, **8**, 2100649.
5 X. Wang, L. Du, L. Cheng, S. Zhai, C. Zhang, W. Wang, Y. Liang, D. Yang, Q. Chen and G. Lei, *Sens. Actuators, B*, 2022, **351**, 130952.
6 Y. Liu and Y. Li, *Sens. Actuators, B*, 2016, **227**, 178–184.
7 S. Kim, Y. Song, H.-R. Lim, Y.-T. Kwon, T.-Y. Hwang, E. Song, S. Lee, Y.-I. Lee, H.-B. Cho and Y.-H. Choa, *Int. J. Hydrogen Energy*, 2017, **42**, 749–756.
8 W.-T. Koo, H.-J. Cho, D.-H. Kim, Y. H. Kim, H. Shin, R. M. Penner and I.-D. Kim, *ACS Nano*, 2020, **14**, 14284–14322.
9 Z. Zhi, W. Gao, J. Yang, C. Geng, B. Yang, C. Tian, S. Fan, H. Li, J. Li and Z. Hua, *Sens. Actuators, B*, 2022, **367**, 132137.
10 A. Dey, *J. Mater. Sci. Eng. B*, 2018, **229**, 206–217.
11 B. Wang, L. Sun, M. Schneider-Ramelow, K.-D. Lang and H.-D. Ngo, *Micromachines*, 2021, **12**, 1429.
12 K. Hu, F. Wang, Z. Shen, Y. Yan and H. Liu, *Int. J. Hydrogen Energy*, 2021, **46**, 20119–20138.
13 Y. Chen, Z. Li, T. Tang, Y. Cheng, L. Cheng, X. Wang, A. A. Haidry, A. Jannat and J. Z. Ou, *ACS Appl. Nano Mater.*, 2024, **7**, 3229–3238.
14 T. Tang, Z. Li, Y. F. Cheng, H. G. Xie, X. X. Wang, Y. L. Chen, L. Cheng, Y. Liang, X. Y. Hu, C. M. Hung, N. D. Hoa, H. Yu, B. Y. Zhang, K. Xu and J. Z. Ou, *J. Hazard. Mater.*, 2023, **451**, 131184.
15 T. Tang, Z. Li, Y. F. Cheng, K. Xu, H. G. Xie, X. X. Wang, X. Y. Hu, H. Yu, B. Y. Zhang, X. W. Tao, C. M. Hung, N. D. Hoa, G. Y. Chen, Y. X. Li and J. Z. Ou, *J. Mater. Chem. A*, 2023, **11**, 6361–6374.
16 F. Favier, E. C. Walter, M. P. Zach, T. Benter and R. M. J. S. Penner, *Science*, 2001, **293**, 2227–2231.
17 F. Yang, S.-C. Kung, M. Cheng, J. C. Hemminger and R. M. Penner, *ACS Nano*, 2010, **4**, 5233–5244.
18 V. Kafil, B. Sreenan, M. Hadj-Nacer, Y. Wang, J. Yoon, M. Greiner, P. Chu, X. Wang, M. S. Fadali and X. Zhu, *Sens. Actuators, A*, 2024, **373**, 115440.
19 I.-D. Kim, A. Rothschild and H. L. J. A. M. Tuller, *Acta Mater.*, 2013, **61**, 974–1000.
20 F. Yang, K. C. Donavan, S.-C. Kung and R. M. Penner, *Nano Lett.*, 2012, **12**, 2924–2930.
21 R. M. Penner, *Acc. Chem. Res.*, 2017, **50**, 1902–1910.
22 G. Li, H. Kobayashi, S. Dekura, R. Ikeda, Y. Kubota, K. Kato, M. Takata, T. Yamamoto, S. Matsumura and H. Kitagawa, *J. Am. Chem. Soc.*, 2014, **136**, 10222–10225.
23 S. K. Konda and A. Chen, *Mater. Today*, 2016, **19**, 100–108.
24 R. Bardhan, A. M. Ruminski, A. Brand and J. J. Urban, *Energy Environ. Sci.*, 2011, **4**, 4882.
25 S. H. Jung, K. Kusakabe, S. Morooka and S.-D. J. Kim, *J. Membr. Sci.*, 2000, **170**, 53–60.
26 J. Catalano, M. Giacinti Baschetti and G. C. Sarti, *J. Membr. Sci.*, 2010, **362**, 221–233.
27 C. P. O'Brien and I. C. Lee, *J. Phys. Chem. C*, 2017, **121**, 16864–16871.
28 D. Gupta, D. Dutta, M. Kumar, P. B. Barman, C. K. Sarkar, S. Basu and S. K. Hazra, *Sens. Actuators, B*, 2014, **196**, 215–222.
29 M.-S. Jo, K.-H. Kim, K.-W. Choi, J.-S. Lee, J.-Y. Yoo, S.-H. Kim, H. Jin, M.-H. Seo and J.-B. Yoon, *ACS Nano*, 2022, **16**, 11957–11967.
30 M.-S. Jo, K.-H. Kim, J.-S. Lee, S.-H. Kim, J.-Y. Yoo, K.-W. Choi, B.-J. Kim, D.-S. Kwon, I. Yoo, J.-S. Yang, M.-K. Chung, S.-Y. Park, M.-H. Seo and J.-B. Yoon, *ACS Nano*, 2023, **17**, 23649–23658.
31 A. Kumar, T. Thundat and M. T. Swihart, *ACS Appl. Nano Mater.*, 2022, **5**, 5895–5905.
32 L. Du and D. Yang, *Appl. Surf. Sci.*, 2023, **607**, 154992.
33 X. Li, T. Cao, X. Zhang, Y. Sang, L. Yang, T. Wang, Y. Li, L. Zhang, L. Guo and Y. Fu, *Sens. Actuators, B*, 2019, **295**, 101–109.
34 S.-Y. Cho, H. Ahn, K. Park, J. Choi, H. Kang and H.-T. Jung, *ACS Sens.*, 2018, **3**, 1876–1883.
35 A. Kumar, M. M. Mohammadi, Y. Zhao, Y. Liu, J. Liu, T. Thundat and M. T. Swihart, *ACS Appl. Nano Mater.*, 2021, **4**, 8081–8093.
36 J. Yun, J.-H. Ahn, D.-I. Moon, Y.-K. Choi and I. Park, *ACS Appl. Mater. Interfaces*, 2019, **11**, 42349–42357.
37 Deepti, H. Kumar, A. Tripathi, A. B. Dey, M. Gupta, R. Krishna and D. K. Avasthi, *Sens. Actuators, B*, 2019, **301**, 127006.
38 L. Du, D. Feng, X. Xing, C. Wang, G. S. Armatas and D. Yang, *Chem. Eng. J.*, 2020, **400**, 125864.
39 W. B. Jung, S. Y. Cho, B. L. Suh, H. W. Yoo, H. J. Jeon, J. Kim and H. T. Jung, *Adv. Mater.*, 2018, **31**, 1805343.
40 W.-T. Koo, Y. Kim, S. Kim, B. L. Suh, S. Savagatrup, J. Kim, S.-J. Lee, T. M. Swager and I.-D. Kim, *Chem*, 2020, **6**, 2746–2758.
41 Q. Liu, J. Yao, Y. Wang, Y. Sun and G. Ding, *Sens. Actuators, B*, 2019, **290**, 544–550.
42 T. A. Peters, P. A. Carvalho, M. Stange and R. Bredesen, *Int. J. Hydrogen Energy*, 2020, **45**, 7488–7496.
43 L. Song, J. Ahn, D.-H. Kim, H. Shin and I.-D. Kim, *ACS Appl. Mater. Interfaces*, 2022, **14**, 28378–28388.
44 K. Yu, X. Tian, X. Wang, F. Yang, T. Qi and J. Zuo, *Sens. Actuators, B*, 2019, **299**, 126989.
45 X. Meng, M. Bi and W. Gao, *Sens. Actuators, B*, 2023, **390**, 133976.
46 Z. Chen, P. Yuan, C. Chen, X. Wang, J. Wang, J. Jia, B. Davaasuren, Z. Lai, N. M. Khashab, K. W. Huang, O. M. Bakr, J. Yin and K. N. Salama, *Adv. Mater.*, 2024, 2404291.
47 H. D. Mai, S. Jeong, T. K. Nguyen, J.-S. Youn, S. Ahn, C.-M. Park and K.-J. Jeon, *ACS Appl. Mater. Interfaces*, 2021, **13**, 14644–14652.
48 M. M. Mohammadi, A. Kumar, J. Liu, Y. Liu, T. Thundat and M. T. Swihart, *ACS Sens.*, 2020, **5**, 2344–2350.
49 B. Xie, B. Ding, P. Mao, Y. Wang, Y. Liu, M. Chen, C. Zhou, H. M. Wen, S. Xia, M. Han, R. E. Palmer, G. Wang and J. Hu, *Small*, 2022, **18**, 2200634.
50 X. Xing, Z. Li, X. Chen, L. Du, Y. Tian, D. Feng, C. Wang, G. Liu and D. Yang, *ACS Appl. Mater. Interfaces*, 2022, **14**, 17911–17919.
51 A. Kumar, Y. Zhao, M. M. Mohammadi, J. Liu, T. Thundat and M. T. Swihart, *ACS Sens.*, 2022, 7, 225–234.
52 J. Hong, S. Lee, J. Seo, S. Pyo, J. Kim and T. Lee, *ACS Appl. Mater. Interfaces*, 2015, **7**, 3554–3561.
53 M. J. López, M. Blanco-Rey, J. I. Juaristi, M. Alducin and J. A. Alonso, *J. Phys. Chem. C*, 2017, **121**, 20756–20762.
54 I. Chakraborty and T. Pradeep, *Chem. Rev.*, 2017, **117**, 8208–8271.
55 L. Geng, Q. Liu, J. Zhao, H. Ye, H. Sun, X. Zhang, P. Zhang, T. Yang, Y. Su, H. Li, D. Zhu, J. Yao, J. Chen, P. Jia, J. Yan, L. Zhang, Y. Tang and J. Huang, *Mater. Today Nano*, 2022, **18**, 100189.
56 D. R. Miller, S. A. Akbar and P. A. Morris, *Sens. Actuators, B*, 2014, **204**, 250–272.
57 Y. Song, F. Chen, Y. Zhang, S. Zhang, F. Liu, P. Sun, X. Yan and G. Lu, *Sens. Actuators, B*, 2019, **287**, 191–198.
58 T. P. Mokoena, H. C. Swart and D. E. Motaung, *J. Alloys Compd.*, 2019, **805**, 267–294.
59 S. U. Mutkule, S. T. Navale, V. V. Jadhav, S. B. Ambade, M. Naushad, A. D. Sagar, V. B. Patil, F. J. Stadler and R. S. Mane, *J. Alloys Compd.*, 2017, **695**, 2008–2015.
60 Z. Li, S. Yan, Z. Wu, H. Li, J. Wang, W. Shen, Z. Wang and Y. Fu, *Int. J. Hydrogen Energy*, 2018, **43**, 22746–22755.
61 H.-J. Kim and J.-H. Lee, *Sens. Actuators, B*, 2014, **192**, 607–627.

62 N. Barsan, C. Simion, T. Heine, S. Pokhrel and U. Weimar, *J. Electroceram.*, 2010, **25**, 11–19.

63 Y. Shen, W. Wang, A. Fan, D. Wei, W. Liu, C. Han, Y. Shen, D. Meng and X. San, *Int. J. Hydrogen Energy*, 2015, **40**, 15773–15779.

64 K. Inyawilert, A. Wisitsoraat, A. Tuantranont, S. Phanichphant and C. Liewhiran, *Sens. Actuators, B*, 2017, **240**, 1141–1152.

65 L. Zhu, W. Zeng and Y. Li, *Mater. Res. Bull.*, 2019, **109**, 108–116.

66 S. Lu, Y. Zhang, J. Liu, H.-Y. Li, Z. Hu, X. Luo, N. Gao, B. Zhang, J. Jiang, A. Zhong, J. Luo and H. Liu, *Sens. Actuators, B*, 2021, **345**, 130334.

67 T. T. Tran, V. Bhatt, M.-J. Choi, H. T. Nguyen, A. Sharma, M. Kumar and J.-H. Yun, *Int. J. Hydrogen Energy*, 2024, **84**, 768–779.

68 I. H. Kadhim, H. A. Hassan and Q. N. Abdullah, *Nano-Micro Lett.*, 2015, **8**, 20–28.

69 Y. Liu, S. Chen, B. Xiao, J. Chu, H. Wang, Y. Chen, T. Yao, A. Yang, X. Han, M. Rong and X. Wang, *Sens. Actuators, B*, 2024, **401**, 135025.

70 Y. Zhang, W. Zeng and Y. Li, *Mater. Res. Bull.*, 2018, **107**, 139–146.

71 Y. Tian, X. Xing, Z. Li, X. Lang, X. Chen, X. Zhao and D. Yang, *Sens. Actuators, B*, 2023, **388**, 133852.

72 X. Zhou, T. Tao, Y. Bao, X. Xia, K. Homewood, Z. Wang, M. Lourenço, Z. Huang, G. Shao and Y. Gao, *ACS Appl. Mater. Interfaces*, 2021, **13**, 25472–25482.

73 X. Zhao, L. Du, X. Xing, Z. Li, Y. Tian, X. Chen, X. Lang, H. Liu and D. Yang, *Small*, 2024, **20**, 2311840.

74 M. Kamal Hossain and Q. Ahmed Drmosh, *Chem. Rec.*, 2022, **22**, e20020090.

75 S. Agarwal, S. Kumar, H. Agrawal, M. G. Moinuddin, M. Kumar, S. K. Sharma and K. Awasthi, *Sens. Actuators, B*, 2021, **346**, 130510.

76 A. Mirzaei, H. R. Yousefi, F. Falsafi, M. Bonyani, J.-H. Lee, J.-H. Kim, H. W. Kim and S. S. Kim, *Int. J. Hydrogen Energy*, 2019, **44**, 20552–20571.

77 D. Degler, U. Weimar and N. Barsan, *ACS Sens.*, 2019, **4**, 2228–2249.

78 N. Yamazoe, G. Sakai and K. Shimanoe, *Catal. Surv. Asia*, 2003, **7**, 63–75.

79 J. Z. Ou, J. L. Campbell, D. Yao, W. Wlodarski and K. Kalantar-zadeh, *J. Phys. Chem. C*, 2011, **115**, 10757–10763.

80 J. Z. Ou, M. H. Yaacob, M. Breedon, H. D. Zheng, J. L. Campbell, K. Latham, J. D. Plessis, W. Wlodarski and K. Kalantar-zadeh, *Phys. Chem. Chem. Phys.*, 2011, **13**, 7330–7339.

81 C. Seo, H. Cheong and S.-H. Lee, *Sol. Energy Mater. Sol. Cells*, 2008, **92**, 190–193.

82 S. K. Deb, *Sol. Energy Mater. Sol. Cells*, 2008, **92**, 245–258.

83 X. Meng, M. Bi, Q. Xiao and W. Gao, *Int. J. Hydrogen Energy*, 2022, **47**, 3157–3169.

84 I. K. Cheng, C.-Y. Lin and F.-M. Pan, *Appl. Surf. Sci.*, 2021, **541**, 148551.

85 A. Sanger, A. Kumar, A. Kumar, J. Jaiswal and R. Chandra, *Sens. Actuators, B*, 2016, **236**, 16–26.

86 Y. Liu, Y. Lei, X. Mao, H. Qian, H.-M. Wen, S. Xia, Y. Xiang, Q. Chen, B. Xie and J. Hu, *Int. J. Hydrogen Energy*, 2024, **62**, 783–793.

87 V. T. Duoc, H. Nguyen, T. M. Ngoc, C. T. Xuan, C. M. Hung, N. V. Duy and N. D. Hoa, *Int. J. Hydrogen Energy*, 2024, **61**, 774–782.

88 Z. Sun, L. Huang, Y. Zhang, X. Wu, M. Zhang, J. Liang, Y. Bao, X. Xia, H. Gu, K. Homewood, M. Lourenco and Y. Gao, *Sens. Actuators, B*, 2024, **398**, 134675.

89 X. Wang, X. Meng and W. Gao, *Sens. Actuators, B*, 2023, **387**, 133790.

90 T. T. D. Nguyen, D. V. Dao, N. Thi Thu Ha, T. Van Tran, D.-S. Kim, J.-W. Yoon, N. N. Ha, I.-H. Lee and Y.-T. Yu, *Sens. Actuators, B*, 2022, **354**, 131083.

91 X. Meng, M. Bi, Q. Xiao and W. Gao, *Sens. Actuators, B*, 2022, **366**, 131971.

92 X. Meng, M. Bi and W. Gao, *Sens. Actuators, B*, 2022, **370**, 132406.

93 G. Pandey, S. D. Lawaniya, S. Kumar, P. K. Dwivedi and K. Awasthi, *J. Mater. Chem. A*, 2023, **11**, 26687–26697.

94 S. Kumar, S. D. Lawaniya, S. R. Nelamarri, M. Kumar, P. K. Dwivedi, Y.-T. Yu, Y. K. Mishra and K. Awasthi, *Sens. Actuators, B*, 2023, **394**, 134394.

95 F. Fan, J. Zhang, J. Li, N. Zhang, R. Hong, X. Deng, P. Tang and D. Li, *Sens. Actuators, B*, 2017, **241**, 895–903.

96 H. Zhao, J. Li, X. She, Y. Chen, M. Wang, Y. Wang, A. Du, C. Tang, C. Zou and Y. Zhou, *ACS Sens.*, 2024, **9**, 2183–2193.

97 A. Vahl, O. Lupan, D. Santos-Carballal, V. Postica, S. Hansen, H. Cavers, N. Wolff, M.-I. Terasa, M. Hoppe, A. Cadi-Essadek, T. Dankwort, L. Kienle, N. H. de Leeuw, R. Adelung and F. Faupel, *J. Mater. Chem. A*, 2020, **8**, 16246–16264.

98 Y.-T. Yu and P. Dutta, *Sens. Actuators, B*, 2011, **157**, 444–449.

99 P. Rai, R. Khan, S. Raj, S. M. Majhi, K.-K. Park, Y.-T. Yu, I.-H. Lee and P. K. Sekhar, *Nanoscale*, 2014, **6**, 581–588.

100 D. Van Dao, T. T. D. Nguyen, T. D. Le, S.-H. Kim, J.-K. Yang, I.-H. Lee and Y.-T. Yu, *J. Mater. Chem. A*, 2020, **8**, 7687–7694.

101 H.-J. Le, D. Van Dao and Y.-T. Yu, *J. Mater. Chem. A*, 2020, **8**, 12968–12974.

102 J. Li, Z. Yuan, Z. Mu, Z. Yang and F. Meng, *Sens. Actuators, B*, 2024, **405**, 135404.

103 H. Chen, Y. Zhao, L. Shi, G.-D. Li, L. Sun and X. Zou, *ACS Appl. Mater. Interfaces*, 2018, **10**, 29795–29804.

104 A. I. Khudiar and A. M. Oufi, *Sens. Actuators, B*, 2021, **340**, 129633.

105 Z. Li, Q. Yang, Y. Wu, Y. He, J. Chen and J. Wang, *Int. J. Hydrogen Energy*, 2019, **44**, 8659–8668.

106 T. Ai, J. Li, S. Nie, Y. Yin, J. Lu, S. Bao and L. Yan, *Int. J. Hydrogen Energy*, 2022, **47**, 20561–20571.

107 M. E. Güldüren, D. İskenderoğlu, H. Güney, E. Gür, M. Acar and S. Morkoç Karadeniz, *Int. J. Hydrogen Energy*, 2023, **48**, 828–839.

108 Y.-J. Hsiao, Y. Nagarjuna, G.-Y. Huang and M. Lin, *J. Alloys Compd.*, 2023, 960.

109 B. Ceviz Şakar, *Int. J. Hydrogen Energy*, 2024, **50**, 1197–1208.

110 S. Kim, G. Singh, M. Oh and K. Lee, *ACS Sens.*, 2021, **6**, 4145–4155.

111 C. Yu, J. Liu, H. Zhao, M. Wang, J. Li, X. She, Y. Chen, Y. Wang, B. Liu, C. Zou, Y. He and Y. Zhou, *IEEE Trans. Instrum. Meas.*, 2024, **73**, 1–8.

112 M. Sun, K. Ding, Y. Lu, X. She, Y. Chen, M. Wang, C. Zou, X. Liu and Y. Zhou, *Microchem. J.*, 2024, 207.

113 Z. Li, Z. Yao, A. A. Haidry, Y. Luan, Y. Chen, B. Y. Zhang, K. Xu, R. Deng, N. Duc Hoa, J. Zhou and J. Z. Ou, *Nano Today*, 2021, **40**, 101287.

114 H. Bai, H. Guo, J. Wang, Y. Dong, B. Liu, F. Guo, D. Chen, R. Zhang and Y. Zheng, *Sens. Actuators, B*, 2021, **331**, 129441.

115 V. Ambardekar, T. Bhowmick and P. P. Bandyopadhyay, *Int. J. Hydrogen Energy*, 2022, **47**, 15120–15131.

116 X.-Y. Zhang, Q. Ren, C. Wang, L. Zhu, W.-J. Ding, Y.-Q. Cao, W.-M. Li, D. Wu and A.-D. Li, *Appl. Surf. Sci.*, 2023, **639**, 157973.

117 Z. Wang, D. Zhang, M. Tang, Y. Chen, Y. Sun, Q. Chen, J. Bian and X. Shao, *Sens. Actuators, B*, 2024, **420**, 136422.

118 Q. Xing, X. Chen, Y. Cai and M. Zhang, *Sens. Actuators, B*, 2024, **419**, 136407.

119 Q. Chen, Y. Zhang, M. Tang, Z. Wang and D. Zhang, *Sens. Actuators, B*, 2024, **405**, 135229.

120 M. P. M. Poschmann, L. Siebert, C. Lupan, O. Lupan, F. Schütt, R. Adelung and N. Stock, *ACS Appl. Mater. Interfaces*, 2023, **15**, 38674–38681.

121 G. Li, Y. Shen, S. Zhao, A. Li, T. Zhao, C. Tang, C. Yan, S. Gao, Z. Yuan and F. Meng, *Sens. Actuators, B*, 2023, **396**, 134560.

122 S. Yang, Z. Chen, Z. Wang, G. Lei, J. Xiong, H. Xu and H. Gu, *Sens. Actuators, B*, 2022, **367**, 132026.

123 X. Wang, X. Meng, Y. Zhu and W. Gao, *Sens. Actuators, B*, 2024, **401**, 134991.

124 P. Ji, X. Hu, R. Tian, H. Zheng, J. Sun, W. Zhang and J. Peng, *J. Mater. Chem. C*, 2020, **8**, 2927–2936.

125 M. Guo, N. Luo, Y. Bai, Z. Xue, Q. Hu and J. Xu, *Sens. Actuators, B*, 2024, **398**, 134151.

126 A. K. Geim and K. S. J. N. m Novoselov, *Nat. Mater.*, 2007, **6**, 183–191.

127 F. Schedin, A. K. Geim, S. V. Morozov, E. W. Hill, P. Blake, M. I. Katsnelson and K. S. Novoselov, *Nat. Mater.*, 2007, **6**, 652–655.

128 J. Z. Ou, W. Ge, B. Carey, T. Daeneke, A. Rotbart, W. Shan, Y. Wang, Z. Fu, A. F. Chrimes and W. Wlodarski, *ACS Nano*, 2015, **9**, 10313–10323.

129 Z. Zhu, X. Ma, C. Liu, S. Liang, S. Xu, L. Wang and J. Xu, *Ceram. Int.*, 2023, **49**, 12840–12845.

130 M. Mehta, Deepti, A. K. Sinha, S. Wadhwa, A. Kumar and D. K. Avasthi, *Int. J. Hydrogen Energy*, 2023, **48**, 33372–33381.

131 B. Lee, S. Cho, B. J. Jeong, S. H. Lee, D. Kim, S. H. Kim, J.-H. Park, H. K. Yu and J.-Y. Choi, *Sens. Actuators, B*, 2024, **401**, 134913.

132 X. Lu, X. Song, C. Gu, H. Ren, Y. Sun and J. Huang, *J. Phys. Chem. Solids*, 2018, **116**, 324–330.

133 N. Kumar, J. Jasani, Y. Sonvane, J. G. Korvink, A. Sharma and B. Sharma, *Sens. Actuators, B*, 2024, **399**, 134807.

134 H. G. Girma, K. H. Park, D. Ji, Y. Kim, H. M. Lee, S. Jeon, S. H. Jung, J. Y. Kim, Y. Y. Noh and B. Lim, *Adv. Funct. Mater.*, 2023, **33**, 2213381.

135 S. Basu and P. Bhattacharyya, *Sens. Actuators, B*, 2012, **173**, 1–21.

136 F.-L. Meng, Z. Guo and X.-J. Huang, *TrAC, Trends Anal. Chem.*, 2015, **68**, 37–47.

137 Y. Xia, R. Li, R. Chen, J. Wang and L. Xiang, *Sensors*, 2018, **18**, 1456.

138 E. Llobet, *Sens. Actuators, B*, 2013, **179**, 32–45.

139 V. Schroeder, S. Savagatrup, M. He, S. Lin and T. M. Swager, *Chem. Rev.*, 2018, **119**, 599–663.

140 D. R. Kauffman and A. Star, *Angew. Chem., Int. Ed.*, 2008, **47**, 6550–6570.

141 L. Du, X. Xing, D. Feng, C. Wang, Z. Li, Y. Tian and D. Yang, *Sens. Actuators, B*, 2023, **375**, 132873.

142 A. Gamboa and E. C. Fernandes, *Sens. Actuators, A*, 2024, **366**, 115013.

143 F. Liu, M. Xiao, Y. Ning, S. Zhou, J. He, Y. Lin and Z. Zhang, *Sci. China Inform. Sci.*, 2022, **65**, 162404.

144 Z. Zhang, Y. Yang, S. Zhu, Y. liu, Y. Shi, J. Song, G. Ren, S. Deng, X. Tian and Z. Zheng, *Int. J. Hydrogen Energy*, 2024, **50**, 870–877.

145 D. Jung, M. Han and G. S. Lee, *ACS Appl. Mater. Interfaces*, 2015, **7**, 3050–3057.

146 B. Liu, M. Alamri, M. Walsh, J. L. Doolin, C. L. Berrie and J. Z. Wu, *ACS Appl. Mater. Interfaces*, 2020, **12**, 53115–53124.

147 Y. Yan, G. Yang, J.-L. Xu, M. Zhang, C.-C. Kuo and S.-D. Wang, *Sci. Technol. Adv. Mater.*, 2021, **21**, 768–786.

148 Y. Da, J. Liu, L. Zhou, X. Zhu, X. Chen and L. Fu, *Adv. Mater.*, 2018, **31**, 1802793.

149 C. Anichini, W. Czepa, D. Pakulski, A. Aliprandi, A. Ciesielski and P. Samorì, *Chem. Soc. Rev.*, 2018, **47**, 4860–4908.

150 T. Minezaki, P. Krüger, F. E. Annanouch, J. Casanova-Cháfer, A. Alagh, I. J. Villar-Garcia, V. Pérez-Dieste, E. Llobet and C. Bittencourt, *Sensors*, 2023, **23**, 4623.

151 Q. Yue, Z. Shao, S. Chang and J. Li, *Nanoscale Res. Lett.*, 2013, **8**, 1–7.

152 C. H. Park, W.-T. Koo, Y. J. Lee, Y. H. Kim, J. Lee, J.-S. Jang, H. Yun, I.-D. Kim and B. J. Kim, *ACS Nano*, 2020, **14**, 9652–9661.

153 J. Jaiswal, P. Tiwari, P. Singh and R. Chandra, *Sens. Actuators, B*, 2020, **325**, 128800.

154 R. Wadhwa, A. Kumar, R. Sarkar, P. P. Mohanty, D. Kumar, S. Deswal, P. Kumar, R. Ahuja, S. Chakraborty, M. Kumar and M. Kumar, *ACS Appl. Nano Mater.*, 2023, **6**, 2527–2537.

155 L. Wang, Z. Xiao, X. Yao, X. Yu, S.-T. Tu and S. Chen, *Int. J. Hydrogen Energy*, 2023, **48**, 30205–30217.

156 C. Qiu, H. Zhang, Q. Li, Y. Song, F. An, H. Wang, S. Wang, L. Zhu, C. Lv and D. Zhang, *Sens. Actuators, B*, 2024, **417**, 136215.

157 M. Naguib, O. Mashtalir, J. Carle, V. Presser, J. Lu, L. Hultman, Y. Gogotsi and M. W. Barsoum, *ACS Nano*, 2012, **6**, 1322–1331.

158 S. Charan, N. Sharma, K. Arjun, S. Mathur, A. K. Vishwkarma and S. Shrivastava, *Int. J. Hydrogen Energy*, 2023, **48**, 38118–38124.

159 M. S. Nam, J.-Y. Kim, A. Mirzaei, H. W. Kim and S. S. Kim, *Sens. Actuators, B*, 2024, **404**, 135189.

160 Z. Zhu, C. Liu, F. Jiang, J. Liu, X. Ma, P. Liu, J. Xu, L. Wang and R. Huang, *J. Hazard. Mater.*, 2020, **399**, 123054.